6436 *Inorg. Chem.* **2009**, *48*, 6436–6451
DOI: 10.1021/ic9002143

Inorganic Chemistry
Article

High- and Low-Temperature Modifications of Sc_3RuC_4 and Sc_3OsC_4—Relativistic Effects, Structure, and Chemical Bonding

Christian Vogt,[†] Rolf-Dieter Hoffmann,[†] Ute Ch. Rodewald,[†] Georg Eickerling,[‡] Manuel Presnitz,[‡] Volker Eyert,[‡] Wolfgang Scherer,*[,‡] and Rainer Pöttgen*[,†]

[†]*Institut für Anorganische und Analytische Chemie, Universität Münster, Corrensstrasse 30, 48149 Münster, Germany, and* [‡]*Institut für Physik, Universität Augsburg, Universitätsstrasse 1, 86159 Augsburg, Germany*

Received February 4, 2009

Sc_3RuC_4 and Sc_3OsC_4 were synthesized by arc-melting and subsequent annealing. At room temperature, they crystallize with the Sc_3CoC_4 structure, space group *Immm*. At 223 and 255 K, Sc_3RuC_4 and Sc_3OsC_4, respectively, show a monoclinic distortion caused by a pair-wise displacement of the one-dimensional $[Ru(C_2)_2]^{\delta-}$ and $[Os(C_2)_2]^{\delta-}$ polyanions, which are embedded in a scandium matrix. Superstructure formation leads to shorter Ru−Ru and Os−Os distances of 316 pm between adjacent $[Ru(C_2)_2]^{\delta-}$ and $[Os(C_2)_2]^{\delta-}$ polyanions. Each ruthenium (osmium) atom is covalently bonded to four C_2 pairs with Ru−C (Os−C) distances of 220−222 pm. A comparison of the C−C bond distances at room temperature in Sc_3TC_4 with *T* representing a group 8 transition metal (Fe, Ru, Os) reveals a minimum in the case of the 4d metal Ru: 144.98(11) pm (Fe), 142.8(7) pm (Ru), and 144.6(4) pm (Os). Analysis of the local electronic structure of the $[T(C_2)_2]$ moieties hints at a complex interplay between chemical bonding and relativistic effects, which is responsible for the V-shaped pattern of the C−C bond distances (long, short, and long for *T* = Fe, Ru, and Os, respectively). Relativistic effects lead to a strengthening of covalent *T*−C bonding. This is shown on the basis of periodic DFT calculations by a significant increase of the charge density at the *T*−C bond critical points ($0.55 < 0.57 < 0.64$ eÅ^{-3}) down the row of group 8 elements. These structural characteristics and topological features do not change in the corresponding low-temperature phases of Sc_3RuC_4 and Sc_3OsC_4. However, topological analyses of theoretical charge density distributions reveal distinct changes of the valence shell charge concentrations at the *transition metal centers* due to the monoclinic distortions. Presumably, the *local* electronic situation at the transition metals reflects the origin and extent of these monoclinic distortions.

Introduction

Scandium carbides have been investigated extensively with respect to their peculiar structural chemistry and chemical bonding features.[1−15] Binary Sc_3C_4 is an outstanding compound, since its structure simultaneously contains isolated carbon atoms besides C_2 pairs and C_3 units,[5,6] separated by scandium atoms. In ternary $Sc_xT_yC_z$ carbides (*T* = transition metal), we observe the formation of covalent *T*−C bonds, leading to one- or two-dimensional $[T_yC_z]$ units which are embedded (1D) or separated (2D) by scandium atoms. Since scandium is smaller than the smallest rare earth (RE) element

*To whom correspondence should be addressed. E-mail: pottgen@uni-muenster.de (R.P.); wolfgang.scherer@physik.uni-augsburg.de (W.S.).

(1) Marusin, E. P.; Bodak, O. I.; Tsokol', A. O.; Baivel'man, M. G. *Kristallografiya* **1985**, *30*, 584–586.
(2) Tsokol', A. O.; Bodak, O. I.; Marusin, E. P. *Kristallografiya* **1986**, *31*, 788–790.
(3) Pecharskaya, A. O.; Marusin, E. P.; Bodak, O. I.; Mazus, M. D. *Kristallografiya* **1990**, *35*, 47–49.
(4) Jeitschko, W.; Gerss, M.; Hoffmann, R.-D.; Lee, S. *J. Less-Common Met.* **1990**, *156*, 397–412.
(5) Pöttgen, R.; Jeitschko, W. *Inorg. Chem.* **1991**, *30*, 427–431.
(6) Hoffmann, R.; Meyer, H.-J. *Z. Anorg. Allg. Chem.* **1992**, *607*, 57–71.
(7) Pöttgen, R.; Jeitschko, W.; Wortmann, U.; Danebrock, M. E. *J. Mater. Chem.* **1992**, *2*, 633–637.
(8) (a) Hoffmann, R.-D.; Pöttgen, R.; Jeitschko, W. *J. Solid State Chem.* **1992**, *99*, 134–139. Indeed, the C−C bond distances in (HT)-Sc_3TC_4 of 144.98(11), 142.8(7), and 144.6(4) pm for *T* = Fe, Ru, and Os, respectively, fall in a narrow range marked by (*i*) transition metal ethyl complexes with shortened C−C single bond distances as a consequence of negative (M−C) hyperconjugation (e.g., 151.26(12) pm in the agostic $(C_2H_5)TiCl_3$(dmpe) complex; dmpe = $Me_2PCH_2CH_2PMe_2$) and (*ii*) transition metal olefin complexes with weakened C═C double bonds due to pronounced M → π^* (C−C) back donation (e.g., 141.89(6) pm in $\eta^2(C_2H_4)$Ni(dbpe); dbpe = $^tBu_2PCH_2CH_2P^tBu_2$). However, the C−C bond distances clearly differ from those of (*iii*) transition metal acetylene complexes displaying C−C triple bonds (e.g. 120.9(1) pm in $[Ag(C_2H_2)Al(OCCH_3(CF_3)_2)_4]$). Note that the C−C bond distances in all of these molecular benchmark systems are directly comparable since they are based on multipolar refinements employing high-resolution X-ray data. Therefore, these distance parameters can be considered as being virtually deconvoluted from thermal smearing effects. See: (b) Scherer, W.; Sirsch, P.; Shorokhov, D.; Tafipolsky, M.; McGrady, G. S.; Gullo, E. *Chem.−Eur. J.* **2003**, *9*, 6057–6070. (c) Scherer, W.; Eickerling, G.; Shorokhov, D.; Gullo, E.; McGrady, G. S.; Sirsch, P. *New J. Chem.* **2006**, *30*, 309–312. (d) Reisinger, A.; Trapp, N.; Krossing, I.; Altmannshofer, S.; Herz, V.; Presnitz, M.; Scherer, W. *Angew. Chem., Int. Ed.* **2007**, *46*, 8295–8298.

 Published on Web 06/12/2009

lutetium,[16,17] the $Sc_xT_yC_z$ carbides mostly form their own structure types. The only exception is the $Sc_5Re_2C_7$ type,[9] which also exists as $RE_5Re_2C_7$ with RE = Er, Tm, and Lu.[18] The largest family among the $Sc_xT_yC_z$ carbides is made up by Sc_3TC_4 with T = Mn, Fe, Co, Ni, Ru, Rh, Os, and Ir.[2,4,8,10,13−15] The structure type was originally determined for Sc_3CoC_4.[2] These carbides contain one-dimensional $[T(C_2)_2]_n^{\delta-}$ polyanionic chains embedded in scandium matrices. Two C_2 pairs connect two transition metal atoms forming "T_2C_4" 1.4 dimetallacycles. The transition metal atom's site symmetry is close to D_{4h} when limited to the first sphere ("TC_4") but reduced to D_{2h} (*mmm*) for the whole chain "$T(C_2)_2$".

The Sc_3TC_4 carbides are highly interesting systems for the investigation of experimental electron density distributions. Recently, we explored the nature of chemical bonding in $Sc_3[Fe(C_2)_2]$ and $Sc_3[Co(C_2)_2]$ by combined experimental and theoretical charge density studies.[14] These analyses revealed substantial T−C bonding within the $T(C_2)_2$ ribbons but also discrete Sc−C bonding of noticeable covalent character. The high-resolution X-ray diffraction data reliably allowed for the experimental distinction of the chemical bonding features of the iron and cobalt carbide with only one electron difference.

In parallel with the diffraction experiments, the Sc_3TC_4 carbides were studied via ^{13}C and ^{45}Sc solid-state NMR.[15] These studies readily revealed two distinct carbon sites in Sc_3RhC_4 and Sc_3IrC_4, while the Sc_3CoC_4 structure type[2] possesses only one independent carbon site. Reinvestigation of the Sc_3RhC_4 and Sc_3IrC_4 structures[13] showed a monoclinic distortion along with a doubling of the unit cell volume, leading to superstructure formation already at room temperature. The distortion is caused by a pairwise dislocation of the rhodium (iridium) atoms off the subcell mirror planes.

In view of the interesting results obtained for Sc_3RhC_4 and Sc_3IrC_4 at room temperature, we were interested in Sc_3RuC_4 and Sc_3OsC_4 with the lower electron count. So far only a room temperature structure refinement has been performed for Sc_3RuC_4.[8,19] The ruthenium atoms showed slightly enhanced U_{11} values; however, there was no need to introduce a split position. Temperature-dependent differential scanning calorimetry of the two carbides gave a hint for a structural phase transition below room temperature. Subsequent temperature-dependent single-crystal X-ray data then gave clear evidence for a monoclinic distortion, however, with a different tilt of the unit cell as compared to Sc_3RhC_4 and Sc_3IrC_4.[13]

Table 1. Lattice Parameters (Guinier Powder Data) of HT-Sc_3RuC_4 and HT-Sc_3OsC_4 at Room Temperature

compound	a / pm	b/pm	c/pm	V/nm^3	ref
HT-Sc_3RuC_4	331.10(4)	448.92(5)	1238.5(1)	0.1841(1)	this work
	331.35(4)	448.77(8)	1238.0(2)	0.1841(1)	ref 8
HT-Sc_3OsC_4	332.71(5)	447.94(7)	1235.7(2)	0.1842(1)	this work
	332.84(5)	448.24(7)	1235.6(2)	0.1843(1)	ref 8

Precise structural data and a detailed analysis of the chemical bonding and its interplay with relativistic effects in the low- and high-temperature modifications of Sc_3RuC_4 and Sc_3OsC_4 are reported herein.

Experimental Section

Synthesis. Starting materials for the preparation of Sc_3RuC_4 and Sc_3OsC_4 were scandium filings (Kristallhandel Kelpin), ruthenium and osmium powder (Degussa-Hüls, ca. 200 mesh), and graphite flakes (Alfa Aesar), all with stated purities better than 99.9%. The elements were mixed in the ideal atomic ratio, cold-pressed to pellets of 6 mm diameter, and arc-melted[20] under an atmosphere of ca. 800 mbar of argon. The argon was purified previously with molecular sieves, silica gel, and titanium sponge (900 K). The samples were remelted several times to ensure homogeneity. The total weight losses were 1 wt % for Sc_3RuC_4 and 3 wt % for Sc_3OsC_4. The larger loss of the osmium compound was due to weak shattering of the brittle sample during remelting. Sc_3RuC_4 and Sc_3OsC_4 are stable in the air for months.

For crystal growth, the arc-melted buttons were sealed in evacuated silica tubes and placed in a water-cooled sample chamber[21] of a rf furnace (Hüttinger Elektronik, Freiburg, TIG 10/500). The best conditions for crystal growth for these high-melting-point carbides is an annealing procedure slightly below the melting point. Therefore, the samples were annealed at the temperature at which the first hints for softening were observed. The power output of the generator was then reduced by approximately 10%, and the buttons were annealed at that power output for 7 and 10 h, respectively.

X-Ray Powder Data. The purity of both samples was controlled by X-ray powder diffraction in a Guinier camera using Cu Kα_1 radiation (λ = 154.056 pm) and α-quartz (a = 491.30, c = 540.46 pm) as an internal standard. The Guinier camera was equipped with an image plate system (Fujifilm, BAS-1800). The orthorhombic lattice parameters at room temperature (Table 1) were obtained by least-squares refinements. The correct indexing of the diffraction lines was ensured through intensity calculations.[22] The obtained values are in good agreement with the data reported previously.[8]

Single Crystal Data. Several small single crystals of Sc_3RuC_4 and Sc_3OsC_4 were isolated from the crushed samples after the annealing procedures. The crystals were glued to small quartz fibers using bees' wax and then examined on a Buerger precession camera (equipped with an image plate system, Fujifilm, BAS-1800) in order to establish their suitability for intensity data collection. First, single-crystal intensity data were collected at room temperature by use of a Stoe IPDS II diffractometer (graphite monochromated Mo Kα radiation) in the oscillation mode. Numerical absorption corrections were applied to the data sets. For the low-temperature data collections, the crystals were mounted on small mechanically rigid glass capillaries. The crystals were first cooled at a rate of 10 K/h to 270 K (Sc_3OsC_4),

(9) Pöttgen, R.; Jeitschko, W. *Z. Naturforsch.* **1992**, *47b*, 358–364.
(10) Wachtmann, K. *Strukturchemische Untersuchungen ternärer Seltenerdmetall- und Actinoid-Carbide mit Haupt- und Nebengruppenelementen*, Dissertation, Universität Münster, Münster, Germany, **1995**.
(11) Pöttgen, R.; Witte, A. M.; Jeitschko, W.; Ebel, Th. *J. Solid State Chem.* **1995**, *119*, 324–330.
(12) Merschrod, E. F.; Courtney, A.; Hoffmann, R. *Z. Anorg. Allg. Chem.* **2002**, *628*, 2757–2763.
(13) Vogt, C.; Hoffmann, R.-D.; Pöttgen, R. *Solid State Sci.* **2005**, *7*, 1003–1009.
(14) Rohrmoser, B.; Eickerling, G.; Presnitz, M.; Scherer, W.; Eyert, V.; Hoffmann, R.-D.; Rodewald, U. Ch.; Vogt, C.; Pöttgen, R. *J. Am. Chem. Soc.* **2007**, *129*, 9356–9365.
(15) Zhang, L.; Fehse, C.; Eckert, H.; Vogt, C.; Hoffmann, R.-D.; Pöttgen, R. *Solid State Sci.* **2007**, *9*, 699–705.
(16) Emsley, J. *The Elements*; Clarendon Press: Oxford, U.K., 1989.
(17) Donohue, J. *The Structures of the Elements*; Wiley: New York, 1974.
(18) Pöttgen, R.; Wachtmann, K. H.; Jeitschko, W.; Lang, A.; Ebel, Th. *Z. Naturforsch.* **1997**, *52b*, 231–236.
(19) Hoffmann, R.-D. *Struktur und Eigenschaften ternärer Lanthanoid-Platinmetall-Carbide*, Dissertation, Universität Münster, Münster, Germany, **1990**.
(20) Pöttgen, R.; Gulden, Th.; Simon, A. *GIT Labor-Fachzeitschrift* **1999**, *43*, 133–136.
(21) Niepmann, D.; Prots', Yu. M.; Pöttgen, R.; Jeitschko, W. *J. Solid State Chem.* **2000**, *154*, 329–337.
(22) Yvon, K.; Jeitschko, W.; Parthé, E. *J. Appl. Crystallogr.* **1977**, *10*, 73–74.

Table 2. Crystal Data and Structure Refinements for the Subcells and the Superstructures of Sc_3RuC_4 and Sc_3OsC_4

refined composition	HT-Sc_3RuC_4	LT-Sc_3RuC_4	HT-Sc_3OsC_4	LT-Sc_3OsC_4
temperature	295 K	100 K	295 K	100 K
formula mass (g mol^{-1})	283.99	283.99	373.12	373.12
space group	*Immm* (No. 71)	*C*12/*m*1 (No. 12)	*Immm* (No. 71)	*C*12/*m*1 (No. 12)
formula units/cell, Z	2	4	2	4
unit cell dimensions (pm)	a = 331.10(4)	a = 1281.4(8)	a = 332.71(5)	a = 1279.5(3)
(295 K: Guinier powder data)	b = 448.92(5)	b = 448.6(1)	b = 447.94(7)	b = 448.56(9)
(100 K: single crystal data)	c = 1238.5(1)	c = 662.7(2)	c = 1235.7(2)	c = 665.3(1)
			β = 104.99(3)°	β = 105.07(1)°
cell volume (nm^3)	V = 0.1841(1)	V = 0.3679(3)	V = 0.1842(1)	V = 0.3687(1)
calculated density (g cm^{-3})	5.12	5.13	6.73	6.72
crystal dimensions (μm)	20 × 40 × 80	15 × 30 × 50	20 × 60 × 100	10 × 70 × 90
range in 2θ	6−70°	6−64°	6−70°	6−64°
detector distance (mm)	60	80	60	80
exposure time (min)	5	15	15	16
ω-range; $\Delta\omega$	0−180°; 1°	0−180°; 1° (ϕ = 0)	0−180°; 1°	3 × 0−180°; 1°
		0−171°; 1° (ϕ = 60°)		(three different ϕ positions)
ϕ positions		0°; 60°		4°; 34°; 64°
integr. param. A; B; EMS	13.5; 3.5; 0.012	11.6; 0.9; 0.022	15.7; 5.0; 0.056	14; 1.5; 0.018
transm. ratio (max/min)	1.35	1.28	3.57	2.91
abs coeff. (mm^{-1})	9.1	9.1	39.5	39.4
F(000)	262	524	326	652
range in *hkl*	$-5 \le h \le +5$	$-18 \le h \le +18$	$-5 \le h \le +5$	$-18 \le h \le +18$
	$-7 \le k \le +7$	$-6 \le k \le +6$	$-7 \le k \le +6$	$-6 \le k \le +6$
	$-19 \le l \le +17$	$-9 \le l \le +9$	$-16 \le l \le +19$	$-9 \le l \le +9$
total no. of reflns	1399	6068	1212	8950
independent reflns	258 (R_{int} = 0.022)	1062 (R_{int} = 0.054)[a]	236 (R_{int} = 0.025)	1042 (R_{int} = 0.032)[a]
reflns with $I > 2\sigma(I)$	226 (R_{sigma} = 0.019)	681 (R_{sigma} = 0.042)	236 (R_{sigma} = 0.015)	878 (R_{sigma} = 0.027)
data/parameter	258/18	1062/37	236/18	1042/37
goodness-of-fit on F^2	1.058	0.889	1.150	1.594
final R indices [$I > 2\sigma(I)$]	R1 = 0.022	R1 = 0.029	R1 = 0.008	R1 = 0.021
	wR2 = 0.055	wR2 = 0.063	wR2 = 0.019	wR2 =0.036
final R indices (all data)	R1 = 0.026	R1 = 0.057	R1 = 0.008	R1 = 0.028
	wR2 = 0.055	wR2 = 0.087	wR2 = 0.019	wR2 = 0.036
BASF		0.501(5)		0.495(3)
extinction parameter	0.030(4)	0.0050(6)	0.0031(6)	0.00137(7)
largest diff. peak/hole	1.50 /−1.32 eÅ^{-3}	1.88/−1.87 eÅ^{-3}	1.03/−0.83 eÅ^{-3}	2.02/−2.53 eÅ^{-3}

[a] Ref 38.

and 240 K (Sc_3RuC_4), that is, close to the phase transition temperature determined by differential scanning calorimetry (DSC; vide infra). Subsequently, the cooling rate was lowered to 2 K/h until a temperature of 170 K was reached, followed by cooling at a rate of 10 K/h down to the measuring temperature of 100 K. Various ϕ positions (Table 2) were chosen in order to increase redundancy and to ensure high-quality numerical absorption corrections. All relevant crystallographic data for the data collections and evaluations are listed in Table 2.

EDX Analyses. The samples were analyzed using a LEICA 420 I scanning electron microscope with Sc, Ru, and Os as standards. No impurity elements heavier than sodium were observed. The detection limit of the instrument did not allow for analyses of the carbon content. The Sc/T ratios determined by EDX were within 2 atom % accuracy (average of the analyses on different points on the surfaces), close to the ideal ratios. The Sc_3RuC_4 sample was highly crystalline. The surface of the arc-melted button consisted of well-shaped columnar single crystals of considerable size (Figure 1).

Differential Scanning Calorimetry. Sc_3RuC_4 and Sc_3OsC_4 were analyzed by DSC using a NETZSCH DSC 204 F1 apparatus. The polycrystalline samples were pressed in small aluminum crucibles, and the subsequent measurements were conducted under a nitrogen atmosphere. The cooling and heating rates were 5 K/min. An empty aluminum crucible was used as reference material, and the apparatus had been calibrated with the reference substances Hg, In, Sn, Zn, Bi, and CsCl. The NETZSCH Proteus software was employed.

Computational Details. Calculations based on the experimental geometries were performed using the scalar-relativistic implementation of the augmented spherical wave (ASW) method.[23,24] In the ASW method, the wave function is expanded in atom-centered augmented spherical waves, which are Hankel functions and numerical solutions of Schrödinger's equation, respectively, outside and inside the so-called augmentation spheres. In order to optimize the basis set, additional augmented spherical waves were placed at carefully

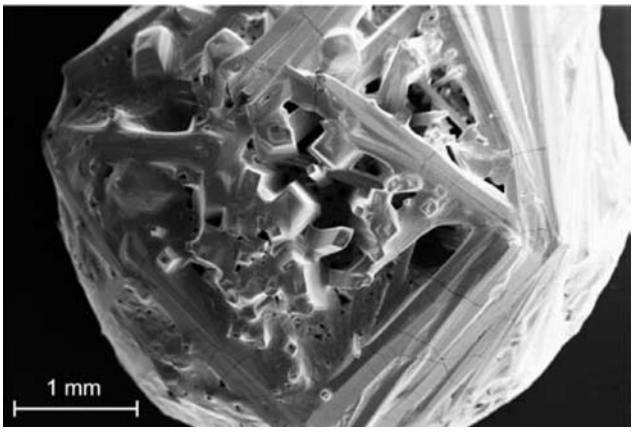

Figure 1. Scanning electron micrograph of an arc-melted button of Sc_3RuC_4. The length scale is given at the lower-left-hand part.

(23) Eyert, V. *Int. J. Quantum Chem.* **2000**, *77*, 1007–1031.
(24) Eyert, V. *The Augmented Spherical Wave Method − A Comprehensive Treatment, Lecture Notes in Physics 719*; Springer: Heidelberg, Germany, 2007; including references therein.

selected interstitial sites. The choice of these sites as well as the augmentation radii were automatically determined using the sphere-geometry optimization algorithm.[25] Self-consistency was achieved by using a highly efficient algorithm for convergence acceleration.[26] The Brillouin zone integrations were performed using the linear tetrahedron method with up to 512 *k* points within the irreducible wedge of the body-centered orthorhombic Brillouin zone.[24,27] In the present work, we used a new full potential version of the ASW method.[28] In this version, the electron density and related quantities are given by a spherical harmonics expansion inside nonoverlapping muffin-tin spheres. In the remaining interstitial region, a representation in terms of atom-centered Hankel functions is used.[29] However, in contrast to previous related implementations, here, a so-called multiple-κ basis set could be avoided, which in fact allows a very high computational speed of the resulting scheme.

For analyses of the topology of theoretical charge density distributions, the WIEN2K program was employed.[30] The calculated charge densities were obtained using the gradient-corrected density functional of Perdew, Burke, and Ernzerhof (PBE)[31] and an augmented plane wave basis set with additional local orbitals (APW + lo). Scalar fields of the negative Laplacian, $L(\mathbf{r}) = -\nabla^2\rho(\mathbf{r})$, were obtained using the LAPW0 routine of the WIEN2K code. The topological parameters at the critical points of the $\rho(\mathbf{r})$ distribution in the framework of Bader's quantum theory of atoms in molecules[32] were obtained either using the implemented atoms in molecules (AIM) routines of the WIEN2K code or by performing numerical analyses of density grid files employing the INTEGRITY program package of Rabillier et al.[33a] However, in maps calculated with a method based on a muffin-tin separation of space as well as on basis functions arising from continuous and differentiable matching at the muffin-tin boundaries (as in WIEN2K), the Laplacian $L(\mathbf{r})$ may show artificial spikes at the surfaces of these spheres. As a consequence, the so-calculated $L(\mathbf{r})$ maps, while being correct in the respective regions of space separately might not be useful for plotting. In this respect, the Sc_3TC_4 carbides (T = Ru, Os) turned out to be extreme cases since the T−C bond critical points (BCPs) nearly lie *on* the muffin-tin spheres of the transition metal atoms. For this reason, we further employed the CRYSTAL06 code,[34] which is based on the linear combination of atomic orbitals approach and thus provides smooth $L(\mathbf{r})$ maps in all regions of space. We therefore employed for calculation of the $L(\mathbf{r})$ maps the CRYSTAL06 code. Here, we also used the PBEPBE functional[31] and employed standard all-electron basis sets: 6-31G for C atoms and 86-411 bases for Sc and Fe ones; the latter are optimized for periodic calculations.[35a−35f] Only in the case of the 4d and 5d metals CRENBL effective core potentials[35g,35h] were used to account also for scalar relativistic effects. For these calculations, the analyses of the charge density distribution were performed numerically via critical point searches as implemented in the INTEGRITY program;[33a] a MATHEMATICA routine written in our group[33b,33c] provided the numerical calculation of $L(\mathbf{r})$ and the ability to create contour plots thereof. Isosurfaces were generally rendered using the program Vmd.[33d]

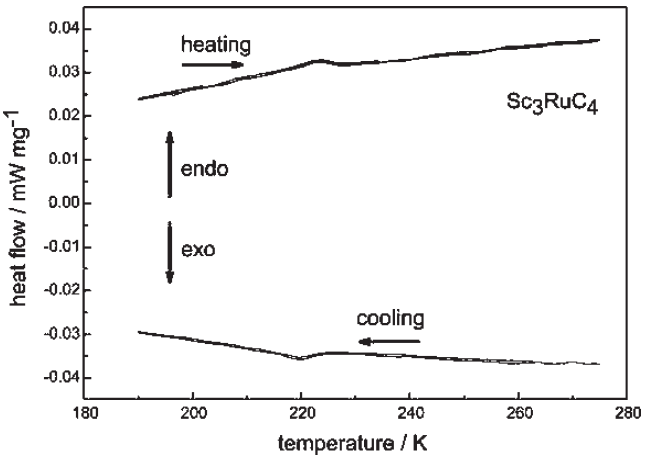

Figure 2. Differential scanning calorimetry measurement for a Sc_3RuC_4 sample in heating and cooling modes.

Results and Discussion

Thermal Behavior. In order to get reliable data for the onset of the structural phase transitions, the Sc_3RuC_4 and Sc_3OsC_4 samples were analyzed by DSC.[36] We present the data for the ruthenium compound in Figure 2. The samples were analyzed in both heating and cooling modes, which show small hystereses. The phase transition temperatures are 223 and 255 K for Sc_3RuC_4 and Sc_3OsC_4, respectively.

Structure Refinements. First, the Sc_3CoC_4-type room-temperature structures in space group *Immm* have been refined. The atomic positions of Sc_3RuC_4 in ref 8 were taken as starting values, and both structures were refined

(25) Eyert, V.; Höck, K.-H. *Phys. Rev. B* **1998**, *57*, 12727–12737.
(26) Eyert, V. *J. Comput. Phys.* **1996**, *124*, 271–285.
(27) Blöchl, P. E.; Jepsen, O; Andersen, O. K. *Phys. Rev. B* **1994**, *49*, 16223–16233.
(28) Eyert, V. To be published.
(29) Methfessel, M. S. *Phys. Rev. B* **1988**, *38*, 1537–1540.
(30) Schwarz, K.; Blaha, P.; Madsen, G.; Kvasnicka, D.; Luitz, J. *WIEN2k*; Technische Universität Wien: Wien, Austria, 2003.
(31) (a) Perdew, J. P.; Burke, K.; Ernzerhof, M. *Phys. Rev. Lett.* **1996**, *77*, 3865–3868. (b) Perdew, J. P.; Burke, K.; Ernzerhof, M. *Phys. Rev. Lett.* **1997**, *78*, 1396.
(32) Bader, R. F. W. *Atoms in Molecules − A Quantum Theory*; Oxford University Press: Oxford, U.K., 1994.
(33) (a) Katan, C.; Rabillier, P.; Lecomte, C.; Guezo, M.; Oison, V.; Souhassou, M. *J. Appl. Crystallogr.* **2003**, *36*, 65–73. (b) *Mathematica*, version 5.2; Wolfram Research, Inc.: Champaign, IL, 2005. (c) Mayer, F.; Herz, V.; Presnitz, M.; Scherer, W. *calc.lap.nb: Mathematica Script for the Analysis of Charge Density Distributions*; Universität Augsburg: Augsburg, Germany, 2007. (d) Humphrey, W.; Dalke, A.; Schulten, K. *J. Mol. Graphics* **1996**, *14*, 33–38.
(34) Dovesi, R.; Saunders, V. R.; Roetti, C.; Orlando, R.; Zicovich-Wilson, C. M.; Pascale, F.; Civalleri, B.; Doll, K.; Harrison, N.; Bush, J.; D'Arco, P.; Llunell, M. *Crystal06*; University Torino: Torino, Italy, 2006.
(35) (a) Hehre, W. J.; Ditchfield, R.; Pople, J. *J. Chem. Phys.* **1972**, *56*, 2257–2261. (b) Schuchardt, K. L.; Didier, B. T.; Elsethagen, T.; Sun, L.; Gurumoorthi, V.; Chase, J.; Li, J.; Windus, T. *J. Chem. Inf. Model.* **2007**, *47*, 1045–1052. (c) Feller, D. *J. Comput. Chem.* **1996**, *17*, 1571–1586. (d) Catti, M.; Valerio, G.; Dovesi, R. *Phys. Rev. B* **1995**, *51*, 7441–7450. (e) Moreira, I. d. P. R.; Dovesi, R.; Roetti, C.; Saunders, V. R.; Orlando, R. *Phys. Rev. B* **2000**, *62*, 7816–7823. (f) Ge, L.; Montanari, B.; Jefferson, J. H.; Pettifor, D. G.; Harrison, N. M.; Briggs, G. A. D. *Phys. Rev. B* **2008**, *77*, 235416. (g) LaJohn, L. A.; Christiansen, P. A.; Ross, R. B.; Atashroo, T.; Ermler, W. C. *J. Chem. Phys.* **1987**, *87*, 2812–2824. (h) Ross, R. B.; Powers, J. M.; Atashroo, T.; Ermler, W. C.; Lajohn, L. A.; Christiansen, P. A. *J. Chem. Phys.* **1990**, *93*, 6654–6670.
(36) The structural phase transitions observed for Sc_3RuC_4 and Sc_3OsC_4 at 223 K and 255 K, respectively, are reflected by sharp peaks in specific heat measurements in the same temperature range. Furthermore, the resistivity curves, $\rho(T)$, reveal an increased metallic behavior for both carbides, which is paralleled by a sharp decrease of the magnetic susceptibility, $\chi(T)$, below the structural phase transition temperature. In the case of the metallic 3d homologue, Sc_3FeC_4, we could not identify any structural phase transition in the temperature range between 1.7 and 300 K. However, its 3d congener, Sc_3CoC_4, shows a pronounced structural phase transition around 60 K and displays superconducting behavior below 3.3 K. Hence, the presence of structural phase transitions in the Sc_3TC_4 carbides seems to be highly correlated with their respective physical properties.

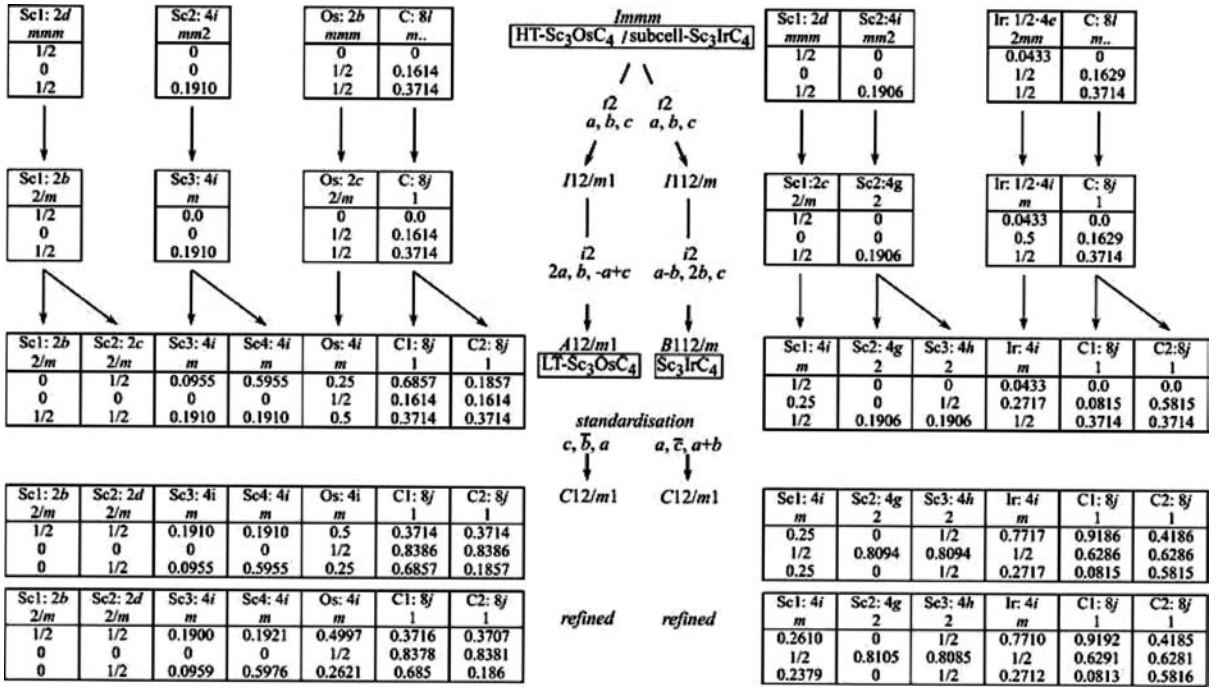

Figure 3. Group−subgroup scheme in the Bärnighausen formalism (refs 40, 41) for the structures of HT-Sc_3OsC_4 (Sc_3CoC_4-type, ref 2), Sc_3IrC_4 (ref 13), and LT-Sc_3OsC_4. The indices for the *translationengleiche* (t) and *isomorphic* (i) symmetry reductions, the unit cell transformations, and the evolution of the atomic parameters are given. In the lower part, the standardization to $C12/m1$ along with the refined data of the superstructures is given.

using the SHELXL-97 code (full-matrix least-squares on F^2)[37] with anisotropic atomic displacement parameters for all atoms. As a check for the correct composition, the occupancy parameters were refined in a separate series of least-squares cycles. All sites were fully occupied within three standard uncertainties. In the final cycles, the ideal occupancies were assumed. The refinements of the room-temperature structures already gave a hint for superstructure formation ($U_{11} > U_{22}$ and U_{33}).

Structure Solution and Refinements of the Low-Temperature Superstructures. On the basis of the results of the room temperature structures, where no superstructure reflections were observed but apparently already "thermal motion" of the T atoms is present, it was assumed that possible phase transitions might occur at lower temperatures for Sc_3RuC_4 and Sc_3OsC_4. Therefore, a crystal of Sc_3OsC_4 was cooled to 150 K to search for superstructure reflections, which indeed could be observed; they were present also at 180 and 235 K. The unit cell of the new superstructure was monoclinic (Table 2) with a doubled volume—one axis was doubled and perpendicular to the doubled axis—a shearing occurred, lowering the symmetry to monoclinic. When the axes were compared with those of Sc_3RhC_4 and Sc_3IrC_4[13], it turned out that the superstructures of Sc_3OsC_4 and isotypic Sc_3RuC_4 follow a different shearing pattern (Figures 3 and 4). The group−subgroup scheme points out that the phase transition might be accompanied by various faults: twinning and antiphase boundaries.

Twinning occurred within the monoclinic plane, simulating additional *doubling* of the subcell c axis. Thus,

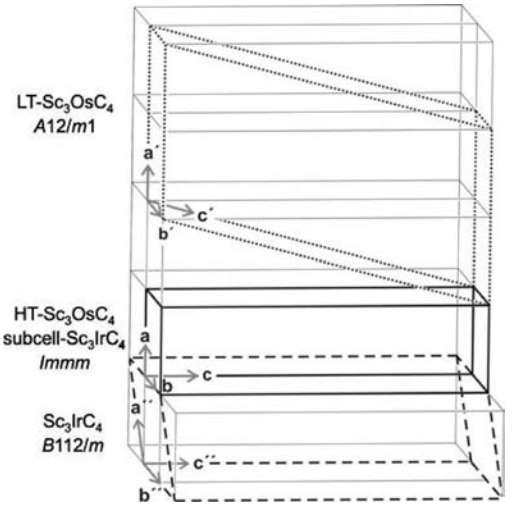

Figure 4. Comparison of the unit cells of HT-Sc_3OsC_4 and Sc_3IrC_4 (subcell), both with the Sc_3CoC_4 structure (continuous line, space group $Immm$) with the two different superstructures realized for LT-Sc_3OsC_4 (dotted line, space group $A12/m1$) and Sc_3IrC_4 (dashed line, space group $B112/m$).

reciprocal space suggested still orthorhombic symmetry because the twin factor can be expected to be close to 0.5. Twinning is hard to suppress, since the symmetry reductions contain a *translationsgleiche* transition of index $t2$, allowing twinning by merohedry due to a change of the crystal system.

A model of the superstructure could be developed with the data set collected at 150 K, but it could not be refined to low residuals (R1 = 0.08) and satisfying displacement parameters. This was in part due to absorption of the large crystal used for the data collection ($20 \times 60 \times 100\ \mu m^3$). Therefore, a smaller crystal ($10 \times 40 \times 50\ \mu m^3$)

(37) Sheldrick, G. M. *SHELXL-97*; University of Göttingen: Göttingen, Germany, 1997.

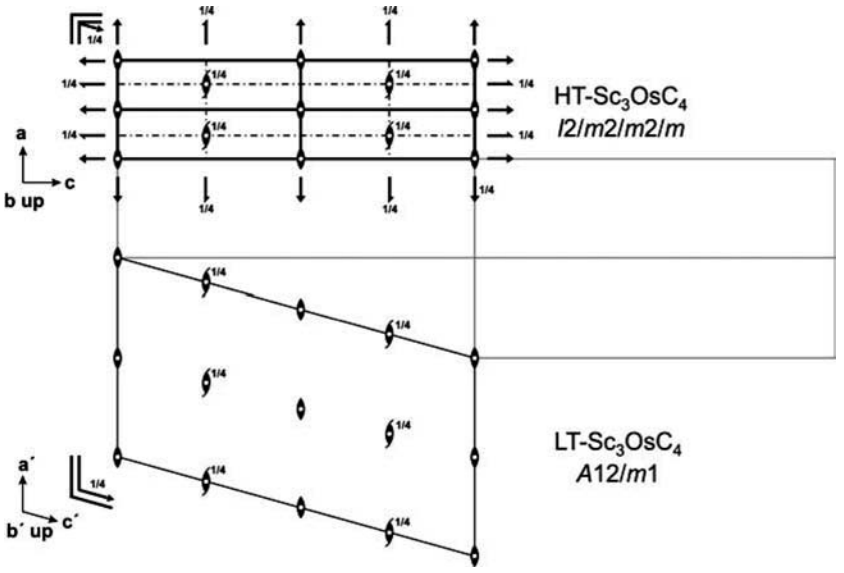

Figure 5. Symmetry thinning related to the formation of the superstructure of LT-Sc_3OsC_4. The intermediate monoclinic space group $I12/m1$ (see Figure 3) is not shown.

of Sc_3OsC_4 was cooled to 100 K, and data were collected while cooling at a rate of 20 K/h. This allowed the phase transition temperature to be narrowed to approximately 250 ± 5 K. Unfortunately, again, this data set did not refine to really satisfying results. The model could be confirmed, but an additional scale factor had to be included to correctly scale between the superstructure reflections of the two twin domains (TDs) and the main overlapping subcell reflections. The additional scale factor essentially corrected for noncoherent scattering within a subcell domain. A subcell domain scatters coherently with respect to the subcell no matter how many twin domains of the superstructure are within a subcell domain. Their number depends on the nucleation processes involved. It can be assumed that a subcell domain contains at least a few TDs separated by twin boundaries (TBs). If the coherent length of a superstructure domain becomes too small, that is, the mean distance between TBs is small, a twin refinement (*hklF* 5 in SHELXL) does not refine well as compared to phase addition. The latter is correct for a disordered model with split positions, as the twin boundaries actually have the symmetry of the subcell. In addition, antiphase boundaries (APBs) might also occur due to the isomorphic (special case of *klassengleiche*) symmetry reduction *i*2 (Figure 3). The latter type of faults usually does not reduce coherent scattering power. However, a high concentration of APB does decrease coherent scattering. As holds true for a TB, also within the area of an APB, only the subcell exists, which explains the scaling problem and ill-behaving displacement parameters.

In order to investigate the nature of the phase transition further, the rapidly cooled crystal of Sc_3OsC_4 was heated in a stepwise manner, while monitoring the intensity of the strongest superstructure reflection. The intensity could be fitted below the transition temperature according to the Landau theory with $I = k(T_c - T)^q$, where k is a scaling parameter, $T_c = 250(1)$ K is the phase transition temperature, T is the temperature in Kelvin, and q is the critical coefficient. Noticeable Bragg intensities or diffuse scattering could not be observed above T_c, ruling out fluctuations of short-range order character. For a second-order transition, q is expected to be 1/2. The fit yielded $q = 0.33(1)$. It was concluded that a second effect, that is, a second length scale for the phase transition, was present, reducing the integral intensity of a superstructure reflection rather than a short-range order effect below T_c as is suggested by a critical coefficient of 1/3. Therefore, the number of APBs presumably had reached a critical concentration. Actually, a TB and an APB can not be distinguished on a microscopic scale for the superstructures. Both originate from the same fault; that is, a transition metal atom (Os) is situated on the wrong side of a subcell mirror plane. However, the propagation of TB and APB is different. Whereas TBs extend in the a/b plane of the subcell, APBs have a phase shift of $a/2$ in the $b/(-a + c)$ plane, as can be deduced from Figures 3 and 5. When going through T_c, the subcell symmetry is broken; the kinetic energy of the transition metal atom does not remain high enough to move all the way through the *broken* mirror plane.

In order to overcome this apparently kinetically controlled boundary problem, that is, too many APBs or too frequently occurring TBs, the same crystal was cooled again, but at 2 K/h (33.3 mK/min), within the critical range of temperatures (vide supra). Proceeding slowly through the phase transition reduces the amount of superstructure domain seeds, since the nucleation depends on the time scale of the cooling procedure. Keeping a low cooling rate below T_c favors Ostwald ripening of the metastable domain structure, meaning domain growth within a superstructure domain and thus reducing APBs. A superstructure domain seed arises from a thermally fixed transition metal atom which does not have enough kinetic energy to move through the subcell mirror plane (those perpendicular to the short a axis). The Boltzmann tail of the energy distribution is responsible for a still large enough number of atoms to swing through, preferable in those areas where the energy is higher due to the additional boundary energy (TBs as well as APBs).

Table 3. Refined Atomic Positions and Displacement Parameters of the High- and Low-Temperature Modifications of Sc_3RuC_4 and Sc_3OsC_4[a]

atom	Wyckoff Pos.	*x*	*y*	*z*	U_{11}	U_{22}	U_{33}	U_{13}	U_{eq}[b]
				HT-Sc_3RuC_4 (295 K, *Immm*)					
Sc1	2*d*	1/2	0	1/2	18(5)	27(5)	24(5)	0	23(2)
Sc2	4*i*	0	0	0.19002(7)	21(4)	20(4)	20(4)	0	20(2)
Ru	2*b*	0	1/2	1/2	82(3)	9(2)	7(2)	0	33(2)
C	8*l*	0	0.1590(8)	0.3708(2)	38(11)	32(11)	21(10)	0	30(5)
				LT-Sc_3RuC_4 (100 K, *C*12/*m*1)					
Sc1	2*b*	0	1/2	0	39(8)	50(8)	31(10)	−3(18)	42(3)
Sc2	2*d*	1/2	0	1/2	42(8)	36(8)	31(10)	1(18)	38(3)
Sc3	4*i*	0.1892(1)	0	0.0905(5)	38(6)	44(6)	24(6)	−8(11)	38(3)
Sc4	4*i*	0.1909(1)	0	0.5917(5)	41(6)	37(6)	31(6)	0(11)	38(3)
Ru	4*i*	0.99973(9)	0	0.26176(8)	29(2)	33(2)	43(3)	7(5)	36(2)
C1	8*j*	0.1287(4)	0.660(1)	0.315(2)	43(6)				
C2	8*j*	0.3702(4)	0.159(1)	0.185(2)	48(6)				
				HT-Sc_3OsC_4 (295 K, *Immm*)					
Sc1	2*d*	1/2	0	1/2	45(2)	48(3)	43(2)	0	45(1)
Sc2	4*i*	0	0	0.19096(4)	46(2)	37(2)	44(2)	0	42(1)
Os	2*b*	0	1/2	1/2	113(1)	26(1)	31(1)	0	56(1)
C	8*l*	0	0.1614(4)	0.3714(1)	66(6)	37(7)	49(6)	0	51(3)
				LT-Sc_3OsC_4 (100 K, *C*12/*m*1)					
Sc1	2*b*	0	1/2	0	14(7)	33(6)	23(8)	−4(15)	25(3)
Sc2	2*d*	1/2	0	1/2	9(7)	10(6)	28(8)	−6(15)	18(3)
Sc3	4*i*	0.1900(1)	0	0.0959(7)	22(5)	19(4)	33(6)	18(10)	23(2)
Sc4	4*i*	0.1921(1)	0	0.5976(7)	26(5)	19(4)	33(6)	20(11)	24(2)
Os	4*i*	0.99968(4)	0	0.26210(3)	16(1)	18(1)	30(1)	3(2)	22(1)
C1	8*j*	0.1284(4)	0.6622(8)	0.315(3)	36(6)				
C2	8*j*	0.3707(4)	0.1619(8)	0.186(3)	34(6)				

[a] The superstructure was refined with the standard setting of the space group *C*2/*m*. [b] U_{eq} is defined as one-third of the derivative of the orthogonalized U_{ij} tensor. The exponent of the anisotropic displacement parameters is defined through $\exp\{-2\pi^2(U_{11}h^2a^{*2} + \ldots + U_{12}hka^*b^*)\}$. $U_{23} = U_{12} = 0$.

Decreasing this energy lets the domains grow. Unfortunately each subcell domain will contain some twin boundaries in the end, leading to a volume ratio of close to 1:1 for the two twin domains.

This slow cooling procedure yielded 100 K data with higher net intensities for the superstructure reflections, lifting the critical exponent to $q = 0.5$. The data could be refined nicely with the results given in Tables 2 and 3. For Sc_3RuC_4, the same procedure was employed except for adapting to the lower phase transition temperature (vide supra). The refinements of the 100 K data of Sc_3OsC_4 and Sc_3RuC_4 were carried out after absorption correction using Laue symmetry 2/*m* for the pseudo-orthorhombic setting (two axes doubled). In the next step, batch numbers for all data were assigned according to the twin law (1 0 0; 0 $\bar{1}$ 0; $\bar{1}$ 0 $\bar{1}$), and the crystal system was changed to monoclinic. The data were merged using MERGEHKLF5.[38] SHELXL *hklF*5 refinements readily converged using damping in the first cycles (damping would later be released). The twin ratios turned out to be close to 0.5, as expected. No additional scaling was necessary; the integral intensity was governed only by the discrete scattering of the two twin domains with nonrelevant contributions of APBs. The critical exponent of 1/2 supports a second-order phase transition at 255 K for Sc_3OsC_4. The same presumably holds true for the phase transition of Sc_3RuC_4 at 223 K.

Final difference electron-density maps for the high- and low-temperature structures did not reveal any significant residual peaks. The results of the structure refinements are summarized in Table 2. The atomic coordinates and the interatomic distances are listed in Tables 3−5. Further information on the structure refinements is available.[39]

Crystal Chemistry. The crystal chemistry and chemical bonding of the subcell structure of the Sc_3CoC_4 type, space group *Immm*, have repeatedly been discussed in previous papers.[2,8,13,14] Herein, we discuss only the structural features of the new low-temperature modification. As is evident from Figures 3−5, we observe a monoclinic distortion through shearing of the unit cell in the *ac* plane. The symmetry is first lowered by a *translationengleiche* reduction of index 2 (t2) from *Immm* to *I*12/*m*1 followed by an isomorphic transition of index 2 (i2) to *A*12/*m*1 upon doubling the *a* axis. The corresponding Bärnighausen tree[40,41] and the evolution of the atomic parameters is shown in Figure 3. The shearing of the unit cell is different for the previously reported superstructures of Sc_3RhC_4 and Sc_3IrC_4.[13] In the latter two carbides, the cell is sheared in the *ab* plane (Figure 4). The thinning of the symmetry from the subcell to the low-temperature structures of Sc_3RuC_4 and Sc_3OsC_4 is shown in Figure 5.

(38) Schreurs, A. M. M. *MERGEHKLF5*; Utrecht University: Utrecht, The Netherlands, 2006.

(39) Details may be obtained from Fachinformationszentrum Karlsruhe, D-76344 Eggenstein-Leopoldshafen (Germany), by quoting the Registry Nos. CSD-420077 (HT-Sc_3RuC_4), CSD-420074 (LT-Sc_3RuC_4), CSD-420076 (HT-Sc_3OsC_4), and CSD-420075 (LT-Sc_3OsC_4).

(40) Bärnighausen, H. *Commun. Math. Chem.* **1980**, *9*, 139–175.

(41) Müller, U. *Z. Anorg. Allg. Chem.* **2004**, *630*, 1519–1537.

Table 4. Interatomic Distances (pm) of HT-Sc_3RuC_4 and HT-Sc_3OsC_4

	HT-Sc_3RuC_4				HT-Sc_3OsC_4		
Sc1:	8	C	241.1(2)	Sc1:	8	C	241.2(1)
	4	Ru	278.91(2)		4	Os	279.0(1)
	4	Sc2	325.21(3)		4	Sc2	325.3(1)
	2	Sc1	331.10(4)		2	Sc1	332.71(5)
Sc2:	2	C	235.0(3)	Sc2:	2	C	234.4(2)
	4	C	237.7(3)		4	C	238.0(1)
	2	Ru	287.7(1)		2	Os	288.72(5)
	4	Sc2	316.01(8)		4	Sc2	314.84(5)
	2	Sc1	325.21(3)		2	Sc1	325.34(5)
	2	Sc2	331.10(4)		2	Sc2	332.71(5)
Ru:	4	C	221.5(3)	Os:	4	C	219.7(2)
	4	Sc1	278.91(2)		4	Sc1	279.0(1)
	4	Sc2	287.7(1)		4	Sc2	288.71(5)
	2	Ru	331.10(4)		2	Os	332.71(5)
C:	1	C	142.8(7)	C:	1	C	144.6(4)
	1	Ru	221.5(3)		1	Os	219.7(2)
	1	Sc2	235.0(3)		1	Sc2	234.4(2)
	2	Sc2	237.7(3)		2	Sc2	238.0(1)
	2	Sc1	241.1(2)		2	Sc1	241.2(1)

The striking structural motifs of the Sc_3RuC_4 and Sc_3OsC_4 structures are one-dimensional infinite ribbons [RuC_4] and [OsC_4], which show a strongly distorted hexagonal rod packing (Figure 6). The [TC_4] ribbons have no interaction with each other. They are completely embedded in a scandium matrix. Exemplarily, we discuss the interatomic distances of the osmium compound. The superstructure contains two crystallographically independent carbon sites. Both carbon atoms form pairs at C−C distances of 145 (C2−C2) and 146 pm (C1−C1), respectively. This C−C bond length is in between a C−C single and double bond, similar to the Sc_3TC_4 compounds with the 3d transition metals.[8,15] The Os−C distances of 220 pm are similar to those of other organometallic compounds, indicating strong covalent Os−C bonding within the ribbons.[42a]

In both superstructures, we observe a puckering of the TC_4 ribbons, but with a different mechanism. In Sc_3IrC_4,[13] the iridium atoms show a pairwise displacement off the subcell mirror planes, leading to alternating shorter and longer Ir−Ir distances between the ribbons. In LT-Sc_3OsC_4, we observe displacements of the complete ribbons toward each other (Figure 7) with inter-ribbon Os−Os distances of 316 and 349 pm, respectively. Even the smaller Os−Os distances are significantly longer than in *hcp* osmium (6 × 267 and 6 × 273 pm),[17] indicating that the superstructure formation is most likely predominantly driven by a geometrical (puckering) effect. On the other side, the formation of the two different superstructures correlates with the electron count.

Electronic Band Structures of Sc_3FeC_4, HT-Sc_3RuC_4, and HT-Sc_3OsC_4. The calculated partial, that is, site- and state-projected, densities of states (DOS) are shown in Figures 8−10 for Sc_3FeC_4, HT-Sc_3RuC_4, and HT-Sc_3OsC_4, respectively. If we consider only the first coordination sphere of the transition metal, namely, the [$T(C_2)_2$] units, the symmetry of the crystal field can be specified by local D_{4h} symmetry.[43] Indeed, the ∠TCC valence angles inside the $T_2(C_2)_2$ units deviate only marginally from 90° (∠TCC = 91.9°, 92.5°, and 92.7° for T = Fe, Ru, and Os, respectively). Therefore, the precise crystallographic site symmetry (*mmm* or D_{2h}) at the transition metal T sites can safely be approximated by D_{4h} symmetry, which will at a later stage allow for a

Table 5. Interatomic Distances (pm) of LT-Sc_3RuC_4 and LT-Sc_3OsC_4[a]

	LT-Sc_3RuC_4				LT-Sc_3OsC_4		
Sc1:	4	C1	241(1)	Sc1:	4	C1	241(1)
	4	C2	241(1)		4	C2	242(1)
	4	Ru	283.59(6)		4	Os	284.15(4)
	4	Sc3	324.2(2)		4	Sc3	324.6(1)
	2	Sc2	331.34(8)		2	Sc2	332.64(5)
Sc2:	4	C1	240(1)	Sc2:	4	C1	241(1)
	4	C2	242(1)		4	C2	241(1)
	4	Ru	274.23(6)		4	Os	274.44(4)
	4	Sc4	325.8(2)		4	Sc4	326.5(1)
	2	Sc1	331.34(8)		2	Sc1	332.64(5)
Sc3:	2	C2	235.1(5)	Sc3:	2	C2	234.9(5)
	2	C2	235(1)		2	C1	237(1)
	2	C1	240(1)		2	C2	238(1)
	1	Ru	289.6(3)		1	Os	292.4(3)
	1	Ru	293.4(3)		1	Os	292.5(3)
	2	Sc3	314.1(4)		2	Sc4	314.1(5)
	2	Sc4	318.6(4)		2	Sc3	316.9(5)
	2	Sc1	324.2(2)		2	Sc1	324.6(1)
	1	Sc4	331.1(2)		1	Sc4	332.2(2)
	1	Sc4	331.6(2)		1	Sc4	333.1(2)
Sc4:	2	C1	234.6(5)	Sc4:	2	C1	233.4(5)
	2	C1	236(1)		2	C2	237(1)
	2	C2	240(1)		2	C1	239(1)
	1	Ru	283.1(3)		1	Os	284.3(3)
	1	Ru	285.3(3)		1	Os	286.1(3)
	2	Sc4	312.3(4)		2	Sc3	314.1(5)
	2	Sc3	318.6(4)		2	Sc4	314.9(5)
	2	Sc2	325.8(2)		2	Sc2	326.5(1)
	1	Sc3	331.1(2)		1	Sc3	332.2(2)
	1	Sc3	331.6(2)		1	Sc3	333.1(2)
Ru:	2	C1	220.9(5)	Os:	2	C1	219.8(4)
	2	C2	221.9(5)		2	C2	220.1(4)
	2	Sc2	274.23(6)		2	Sc2	274.44(4)
	1	Sc4	283.1(3)		2	Sc1	284.15(4)
	2	Sc1	283.59(6)		1	Sc4	284.3(3)
	1	Sc4	285.3(3)		1	Sc4	286.1(3)
	1	Sc3	289.6(3)		1	Sc3	292.4(3)
	1	Sc3	293.4(3)		1	Sc3	292.5(3)
	1	Ru	315.6(1)		1	Os	316.32(6)
C1:	1	C1	143.6(9)	C1:	1	C1	145.5(8)
	1	Ru	220.9(5)		1	Os	219.8(4)
	1	Sc4	234.6(5)		1	Sc4	233.4(5)
	1	Sc4	236(1)		1	Sc3	237(1)
	1	Sc3	240(1)		1	Sc4	239(1)
	1	Sc2	240(1)		1	Sc2	241(1)
	1	Sc1	241(1)		1	Sc1	241(1)
C2:	1	C2	142(1)	C2:	1	C2	145.2(8)
	1	Ru	221.9(5)		1	Os	220.1(4)
	1	Sc3	235.1(5)		1	Sc3	234.9(5)
	1	Sc3	235(1)		1	Sc4	237(1)
	1	Sc4	240(1)		1	Sc3	238(1)
	1	Sc1	241(1)		1	Sc2	241(1)
	1	Sc2	242(1)		1	Sc1	242(1)

[a] All distances within the first coordination spheres are listed. Standard deviations are given in parentheses.

(42) (a) A search in the Cambridge Structural Database (CSD version 5.30, November 2008) results in 114 deposited X-ray structures containing an Os−C≡C fragment displaying an average Os−C distance of 214.7 pm. (b) The corresponding C−C bond lengths of the group 9 transition metal carbides Sc_3TC_4 are comparable: 145.39(8) pm (Co), 142.4(11) and 142.5 (10) pm (Rh), and 144.4(8) and 145.3(8) pm (Ir).

(43) Indeed, analysis of the d-orbital population derived from the experimental multipolar model of Sc_3FeC_4 showed that the cross terms $P(3z^2 - r^2/xy) = -0.19(20)$ and $P(xz/yz) = 0.12(21)$ are not significantly populated (see ref 14).

comparison with the electronic situation in d^8 ML_4 complexes (M = transition metal, L = ligand; cf. Figure 15, vide infra). Note that, in assigning the crystal orbitals, we used a rotated reference frame with the local z axis perpendicular to the T−C planes and the x axis pointing along one of the T−C bonds. The y axis closely approximates another T−C bond of the $[T(C_2)_2]$ units (see Figure 15, vide infra).

The results look very similar to those presented in our previous work on Sc_3FeC_4 and Sc_3CoC_4.[14] However, there exist slight differences due to the fact that, in the previous work, the full-potential ASW method was not yet available, and we thus had to use a simplified methodology based on the atomic sphere approximation. In the shown range of partial densities of states (Figure 8), four energy regions can be distinguished. In the least populated interval from −10 to −7 eV, mainly C p_x and p_y and Sc 3d states are observed with an admixture of Fe $3d_{x^2-y^2}$ states at about −8 eV. The carbon states also dominate the interval from −7 to about −3 eV. However, there are again admixtures from the other atoms, mainly from Fe $3d_{x^2-y^2}$ states of b_{1g} symmetry (see also Figure 14a for a simplified DOS diagram). The latter contributions are due to the strong σ-type bonding between these orbitals and the in-plane carbon p orbitals, as indicated by the peak at about −4.5 eV visible in both types of partial DOS. The corresponding antibonding peak is clearly observable at 1.8 eV. The interval from −3 to about 1 eV is characterized mostly by Fe 3d states. Finally, at energies above 1 eV, the main contribution of the Sc 3d states sets in.

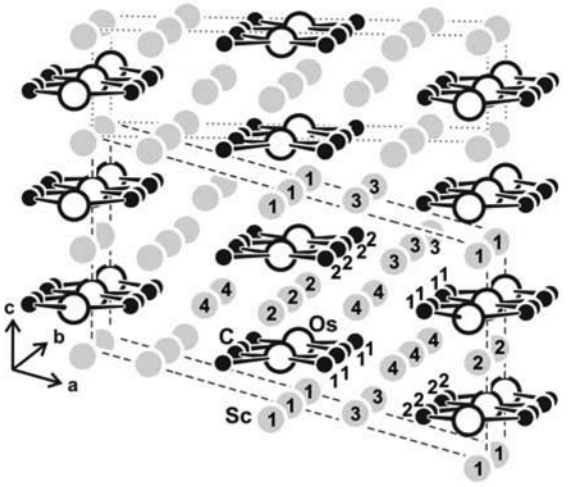

Figure 6. View of the LT-Sc_3OsC_4 structure (unit cell in dashed line) approximately along the b axis. Scandium, osmium, and carbon atoms are drawn as medium gray, open, and black filled circles, respectively. The subcell (dotted lines), the one-dimensional $[OsC_4]$ polyanions, and the crystallographically independent scandium sites are indicated.

Worth mentioning is the strong Fe $3d_{xy}$ peak at about −0.6 eV. These d orbitals of b_{2g} symmetry do not participate significantly in covalent bonding, hence, their sharp structure. However, the small but distinct splitting of this peak might be reminiscent of small metal−metal bonding along the direction of the ribbons. We also point to the strong splitting of the Fe $3d_{3z^2-r^2}$ states of a_{1g} symmetry into two sharp peaks at −1.9 eV and just below the Fermi level, which are complemented by peaks in the C p_z partial DOS and reflect, for symmetry reasons, basically nonbonding interactions between these orbitals. However, the Fe $3d_{3z^2-r^2}$ orbitals also contribute (to a lesser extent relative to the Fe $3d_{x^2-y^2}$ states) to covalent σ(Fe−C) bonding with the C p_x and p_y orbitals, as signaled by a sharp DOS feature at −2.7 eV in combination with the corresponding antibonding peak at 1.8 eV. Furthermore, we find some minor contributions of s and p_x/p_y metal states to the global T−C bonding. Pronounced π(Fe−C) bonding, however, is reflected by a sharp feature at −2.1 eV involving the out-of-plane C $2p_z$ orbitals and the Fe d_{xz} and d_{yz} orbitals, which are of e_g symmetry. This type of π-type

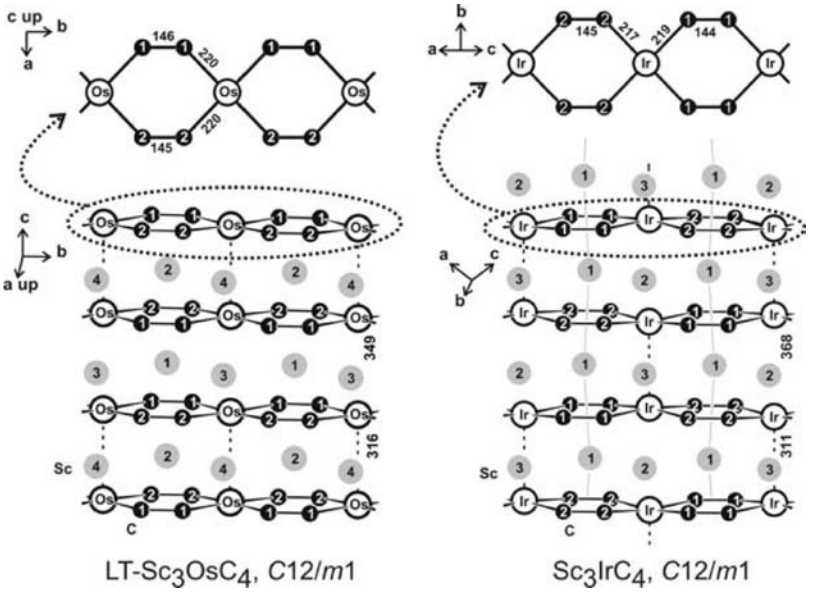

Figure 7. The two different structural distortions of the superstructures of the Sc_3CoC_4 type, the LT-Sc_3OsC_4 (left-hand side) and the Sc_3IrC_4 (right-hand side) types. Scandium, osmium (iridium), and carbon atoms are drawn as medium gray, open, and black filled circles, respectively. Atom designations and relevant interatomic distances (in pm) are indicated.

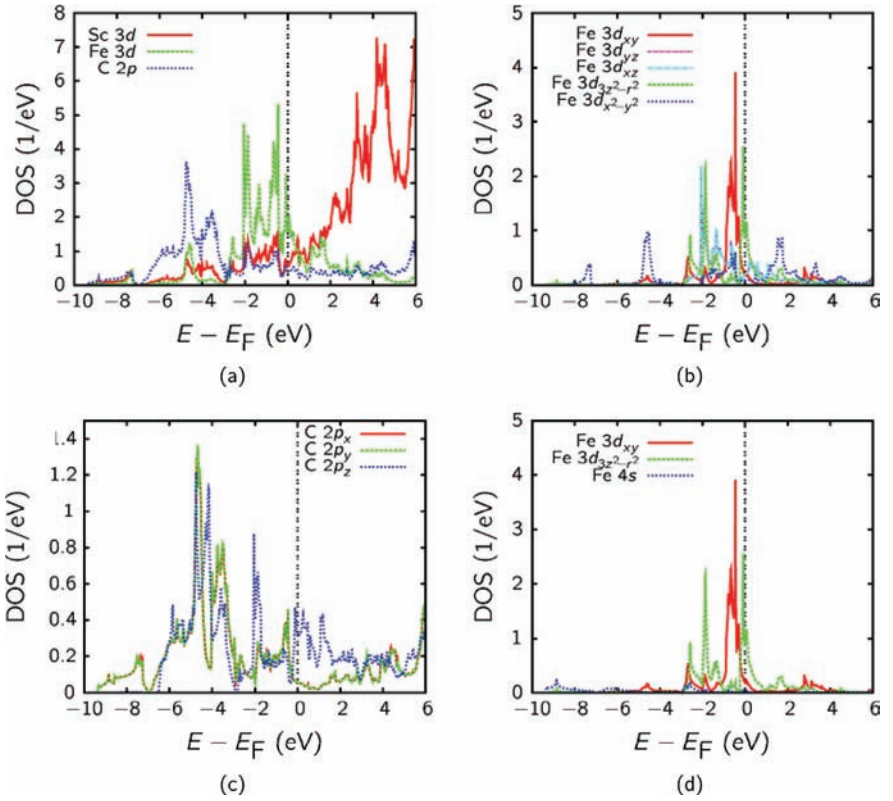

Figure 8. Site- and state-projected partial densities of states (DOS) of Sc_3FeC_4.

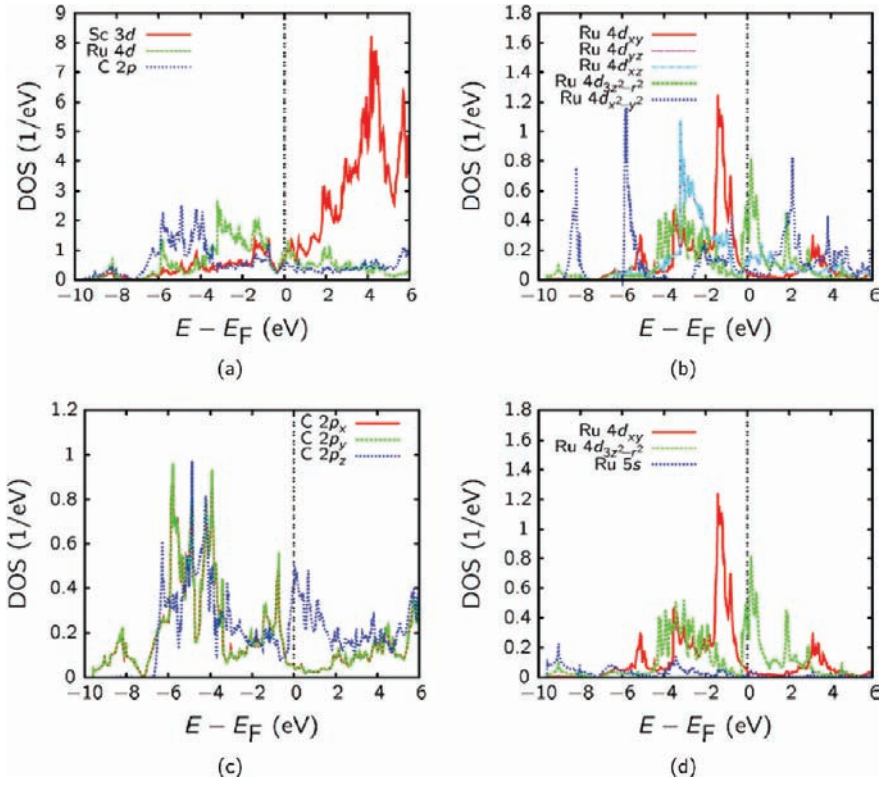

Figure 9. Site- and state-projected partial densities of states (DOS) of HT-Sc_3RuC_4.

overlap is responsible for the back-donation of charge from the e_g-type orbitals to the C−C antibonding π^* states of the C_2 units. Such π-type bonding must be oriented out-of-plane of the [FeC_4] units. Hence, all Fe 3d states except the d_{xy} one are involved in chemical bonding.

The electronic situation is similar for Sc_3RuC_4 and Sc_3OsC_4. For these two compounds, the partial DOS

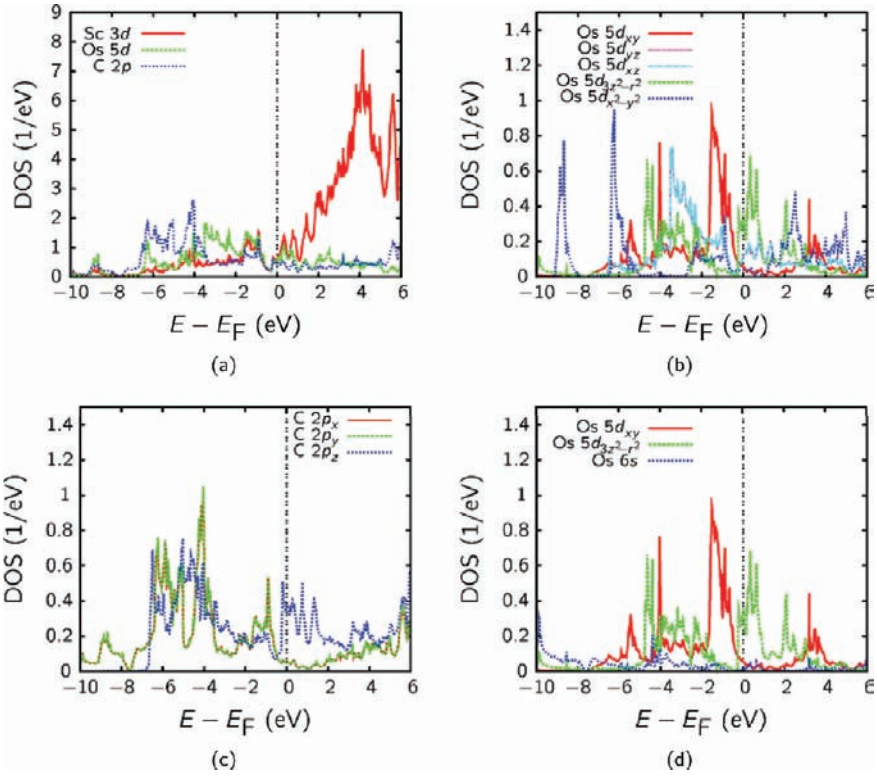

Figure 10. Site- and state-projected partial densities of states (DOS) of HT-Sc_3OsC_4.

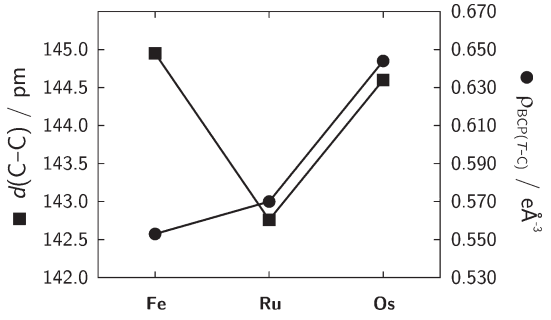

Figure 11. Experimental C−C bond lengths (squares) in picometers and theoretical (WIEN2K calculations) charge density accumulation (circles) in $e\text{Å}^{-3}$ at the T−C bond critical points for T = Fe, Ru, and Os.

are displayed in Figures 9 and 10, respectively. Again, we are able to identify four different energy windows extending approximately from −10 to −7 eV, from −7 to −3.5 eV, from −3.5 to −0.3 eV, and from −0.3 to 6.0 eV. The first window is characterized by an admixture from all three atomic species, the following ones by dominant carbon, Ru/Os, and scandium states, respectively. However, the groups of bands have broadened, and their energetic separation is generally somewhat reduced. This is a consequence of the larger spatial extent of the 4d and 5d states as compared to the 3d states. For the same reason, the peak heights of the Ru/Os d partial DOS are likewise reduced as compared to the Fe d partial DOS (Figure 8). This is particularly true for the strong $d_{3z^2-r^2}$ peaks at −1.9 eV and just below the Fermi energy as well as for those peaks at −2.1 eV due to the d_{xz} and d_{yz} orbitals, which have been considerably broadened in the case of the heavier congeners Ru and Os. The major difference in the electronic structure on exchanging the transition metal atom is a larger separation between bonding and antibonding $\sigma(T-C)$ levels down the row of the group 8 metals: −4.5 to 1.8 eV (Fe), −5.5 to 2.2 eV (Ru), and −6.5 to 2.5 eV (Os). This gap increase correlates with an increase of covalent $\sigma(T-C)$ bonding—in line with the topological analysis of the charge density distribution at the respective T−C bond critical points (vide infra).

Chemical Bonding Analysis and Relativistic Effects. We first consider the T−C bonding within the $[T(C_2)_2]$ moiety in Sc_3FeC_4 and in the HT phases of Sc_3RuC_4 and Sc_3OsC_4 in more detail. Analysis of the charge density distribution at the T−C BCPs reveals a clear trend of increasing $\rho(\mathbf{r}_c)$ values from T = Fe to T = Os (Figure 11 and Table 6). This again clearly suggests an increase of the T−C bond strength down the row of the group 8 elements. Accordingly, the splitting of the $\sigma(T-C)$ bonding and antibonding states (vide supra) which becomes larger from T = Fe to T = Os can be correlated with a respective strengthening of the T−C bonds. These findings, therefore, support our suggestion that the Os−C distances of about 220 pm signal covalent Os−C bonding.[42a] We further note the good agreement between the topological parameters derived with the WIEN2K and CRYSTAL06 code (Table 6). However, if not specified otherwise, the WIEN2K calculations will be our default method in the following.

The bonding situation becomes more complex if we also consider the trends reflected by the C−C distances of the $(C_2)^{2-}$ moieties. The C−C bond distances at RT reveal a minimum in case of the 4d metal ruthenium: 144.98(11) pm (Fe), 142.8(7) pm (Ru), and 144.6(4) pm (Os) (Figure 11).[42b] The C−C distances are in between a C−C single and double bond and are controlled by

Table 6. Analysis of Bond and Ring CPs in Sc_3TC_4, (T = Fe, Ru, and Os)[a]

	HT modification			LT modification		
unit	distance	$\rho(\mathbf{r}_c)^b$	$\nabla^2\rho(\mathbf{r}_c)^b$	distance	$\rho(\mathbf{r}_c)^b$	$\nabla^2\rho(\mathbf{r}_c)^b$
Fe−C1[c]	210.74(6)	0.553 [0.566]	4.5 [4.9]			
Ru−C1	221.5(3)	0.570 [0.583]	4.8 [4.8]	220.9(5)	0.584 [0.589]	4.6 [4.9]
Ru−C2				221.9(5)	0.574 [0.580]	4.6 [4.8]
Os−C1	219.7(2)	0.644 [0.637]	5.1 [5.1]	219.8(4)	0.652 [0.636]	4.7 [5.2]
Os−C2				220.1(4)	0.648 [0.632]	4.6 [5.1]
(Fe) C1−C1	144.98(11)	1.765 [1.654]	−14.8 [−9.5]			
(Ru) C1−C1	142.8(7)	1.821 [1.736]	−19.0 [−11.1]	143.6(9)	1.825 [1.708]	−18.9 [−10.0]
C2−C2				142(1)	1.869 [1.741]	−20.1 [−11.0]
(Os) C1−C1	144.6(4)	1.770 [1.671]	−17.9 [−9.9]	145.5(8)	1.753 [1.640]	−17.5 [−9.5]
C2−C2				145.2(8)	1.763 [1.650]	−17.8 [−9.7]

[a] The charge density, $\rho(\mathbf{r}_c)$, is given in eÅ^{-3}, $\nabla^2\rho(\mathbf{r}_c)$ in eÅ^{-5}; all distances in pm. [b] These theoretical values are based on the WIEN2K results; values based on CRYSTAL06 results in square brackets. [c] Data were taken from ref 14.

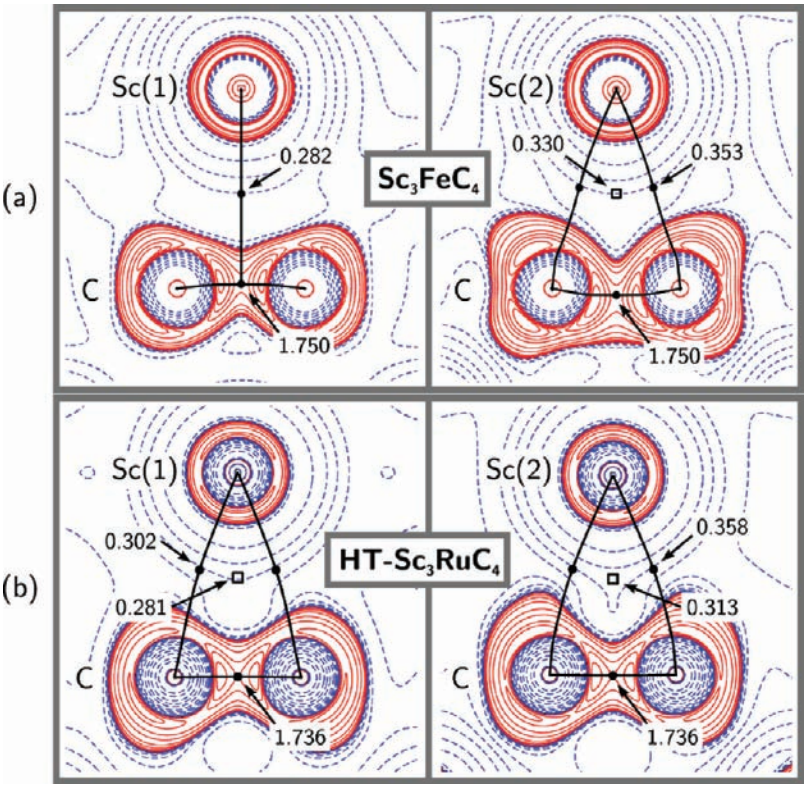

Figure 12. Contour maps of $L(\mathbf{r}) = -\nabla^2\rho(\mathbf{r})$ showing the bond path in the Sc(1)C_2 fragments (left) and Sc(2)C_2 fragments (right), obtained from (a) experimental charge density studies of Sc_3FeC_4 (ref 14) and (b) DFT calculations using the CRYSTAL06 code for Sc_3RuC_4 (details see main text), respectively. A T-type bond path is only observed for the Sc(1)C_2 bond in Sc_3FeC_4. Contour levels are drawn at $\pm m \times 10^{\pm n}$ eÅ^{-5}, where m = 2, 4, 8 and n = 0, 1, 2, 3. Extra levels at (a) 11, 15, 1200, and 1500; (b) 11, 15, and 145 eÅ^{-5}. Positive and negative values are marked by solid and dashed lines, respectively. BCPs and ring critical points (RCPs) are marked by closed circles and open squares, respectively. The magnitudes of the BCPs and RCPs are specified in eÅ^{-3}. T-type and exocyclic Sc−C bond paths are marked by solid lines.

$T \rightarrow \pi^*$(C−C) back-donation involving the out-of-plane C 2p$_z$ orbitals and the T d$_{xz}$ and d$_{yz}$ orbitals (Figure 14a,c, vide infra).[8,14] The C−C bond distances are also affected by Sc(C_2) interactions. Indeed, our experimental charge density study on Sc_3FeC_4 provided clear evidence for a side-on complexation of the Sc(2) atoms by the C_2 unit (Figure 12a).[14] This result is supported by the WIEN2K and CRYSTAL06 calculations (the latter shown in Figure 12b) which further predict the existence of cyclic Sc(2)C_2 bond paths, also in case of the Ru and Os carbides. The presence of two separated Sc(2)−C bond paths suggests covalent metallacyclopropane-type bonding contributions in all three carbides Sc_3TC_4 (T= Fe, Ru, Os).[8c,8d,14,44] In the case of the Sc(1)$\cdots$(C_2) interactions, the situation is less clear (Figure 12). The WIEN2k calculations suggest a T-shaped bond path for the 3d and 4d transition metal carbides and a cyclic one (with a minute splitting of both Sc(1)−C BCPs) in the case of

(44) (a) Macchi, P.; Proserpio, D. M.; Sironi, A. *J. Am. Chem. Soc.* **1998**, *120*, 1447–1455. (b) Hertwig, R. H.; Koch, W.; Schröder, D.; Schwarz, H.; Hrušák, J.; Schwertfeger, P. *J. Phys. Chem.* **1996**, *100*, 12253–12260. (c) Frenking, G.; Fröhlich, N. *Chem. Rev.* **2000**, *100*, 717–774. (d) Himmel, D.; Trapp, N.; Krossing, I.; Altmannshofer, S.; Herz, V.; Eickerling, G.; Scherer, W. *Angew. Chem., Int. Ed. Engl.* **2008**, *47*, 7798–7801. (e) Krapp, A.; Frenking, G. *Angew. Chem., Int. Ed.* **2008**, *47*, 7796–7797. (f) Bader, R. F. W.; Nguyen-Dang, T. T.; Tal, Y. *Rep. Prog. Phys.* **1981**, *44*, 893–948.

Scheme 1

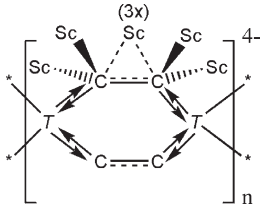

Sc_3OsC_4. This may indicate that electrostatic interactions dominate the Sc(1)−C interaction while covalent bonding prevails in the cyclic $Sc(2)C_2$ moieties.[44d,44e] However, the CRYSTAL06 calculations predict cyclic bond paths for all $Sc(1)C_2$ moieties in Sc_3TC_4 (T = Fe, Ru, Os; Figure 12b). Hence, subtle changes in the level of approximation employed might render the T-shaped bond path in the $Sc(1)C_2$ moieties into a metalla-cyclic one and vice versa. As a consequence of both σ donor and π back-bonding in these $Sc(1)C_2$ moieties, only small charge density differences are present between the ring and bond critical points (Figure 12), which is indicative of a structurally unstable situation close to a catastrophe point,[44f] rendering the cyclic bond path in a T-type one and vice versa. This renders the discrimination of both types of ScC_2 bond path topologies somewhat difficult. Accordingly, the $Sc(2)C_2$ and $Sc(1)C_2$ moieties are both characterized by a similar (weak) extent of Sc−C bond covalency.

We can conclude that the C−C bond lengths of the $(C_2)^{2-}$ units are primarily controlled by covalent (*i*) $\sigma(T \leftarrow C)$ donation, (*ii*) $T \rightarrow \pi^*(C-C)$ back-donation, and (*iii*) partially covalent $Sc(\eta^2(C_2))$ bonding (Scheme 1). Thus, the $[T(C_2)_2]^{4-}$ units might be formally interpreted as the first examples of an organometallic $T(d^8)$ tetraalkylidene species if we neglect the partial oxidation of the metal center (e.g., $Q_{AIM}(Fe) = +0.50/+0.15e$ in experiment and theory, respectively).[14,45]

We note that our Sc_3TC_4 bonding description is related to Halet's model[46] developed for dicarbides encapsulated in metal clusters, where the C_2 units are formally considered as dianionic species and act as eight-electron donors. This consideration is in agreement with the octet rule and the AIM charges of the $(C_2)^{2-}$ moieties in Sc_3FeC_4 ($Q_{AIM}(C) = -0.99/-1.3e$ in experiment and theory, respectively).[14] Hence, the variation of the C−C distances depends basically on the electronic effects coming from the metallic environment. Similar C−C distances can also be found for C_2 units encapsulated in metal clusters: for example, $Co_6(C_2)(CO)_{18}$ (prismatic Co_6 coordination; C−C = 142.6(9) pm)[47a] and $[Co_9(C_2)(CO_{19})]^{2-}$ (tricapped Co_9 prism; C−C = 139(2) pm).[47b]

However, both bonding concepts do not explain the V-shaped pattern of (long, short, and long) C−C bond distances in the series of group 8 transition metal carbides (Figure 11). A similar scenario was previously predicted by Ziegler and co-workers in the case of 3d, 4d, and 5d transition metal acetylene complexes $M(C_2H_2)$, where M represents a group 10 element.[48] A more recent theoretical study of the $M(C_2H_2)$ benchmark systems[44d,49] showed that not only the C−C distances but also the BCP characteristics were similar for the 3d and 5d metals Ni and Pt (128.2 pm/2.52 eÅ^{-3} and 128.5 pm/2.52 eÅ^{-3}, respectively), while for the 4d element Pd, a significantly shorter bond distance of 126.5 pm and a larger charge accumulation at the BCP of 2.61 eÅ^{-3} was calculated. Also, the precise structural data of the organometallic $Sc_3[T(C_2)_2]$ carbides suggest that the observed V-shaped pattern of C−C bond distances is due to relativistic effects. Here, the structural trends in C−C bond distances are also reflected by the topology of the electron density at the C−C BCPs (Table 6). We find that $\rho(\mathbf{r})$ at the BCP is higher for the shorter C−C bonds in the Ru compound (1.82 eÅ^{-3}) compared to the value found for the longer C−C bonds for T = Fe and Os (1.77 eÅ^{-3} in both cases). This result suggests that $T \rightarrow \pi^*(C-C)$ back-donation is less pronounced in the case of 4d row transition elements in the $[T(C_2)_2]$ moieties of solid carbides. We note that this interpretation is in agreement with Ziegler's interpretation of the V-shaped C−C bond distance pattern displayed by the $M(C_2H_2)$ benchmark systems. Hence, both nonperiodic trends in *molecular acetylene* complexes and *solid acetylides* could be caused by relativistic effects—a result which warrants further exploration.

Another indicator for the presence of relativistic effects is evident from the larger energy separation of the nonbonding $T\,d_{xy}$ and $T\,d_{3z^2-r^2}$ states in $Sc_3[T(C_2)_2]$: ∼0.6 eV (Fe), ∼1.6 eV (Ru), and ∼2.0 eV (Os) (Figures 8−10 and 13a,c). In general, the relativistic contraction and energetic stabilization of the s-type orbitals leads to a reduction of the effective atomic charge seen by the d electrons and raises their energy.[48,50] According to relativistic atomic calculations by Ziegler and co-workers, the Os 6s atomic orbital is lowered by 1.07 eV, whereas the 5d orbital is raised by 1.79 eV. We suggest that the increasing gap between the $T\,d_{xy}$ and $T\,d_{3z^2-r^2}$ states down the row of group 8 elements is due to a strong mixing of the T (n)s states and the T ($n-1$)d_{xy} states. This mixing is allowed by symmetry and maintains the nonbonding character of these hybrid states (Figure 14). In the case of the $T\,d_{3z^2-r^2}$ states, s/d mixing is also allowed for symmetry reasons, but these states are situated mainly above the Fermi level for T = Ru and Os and remain virtually unpopulated. As a consequence of the formation of these s/d_{xy} hybrid states, we observe an asymmetry of the four equatorial charge concentrations in the valence shell of the transition metal atoms T. This is exemplified in Figure 14c in case of the HT and LT variants of Sc_3RuC_4.

(45) The existence of square planar organometallic $[FeR_4]^{4-}$ (R = alkyl, phenyl) complexes has been claimed for decades in the chemical literature. However, the celebrated example of such an $Fe(d^8)$ species $[Li(Et_2O)]_4[FePh_4]$ turned out to be most likely a case of a mistaken identity ($[Li(Et_2O)]_4[FeH_2Ph_4]$). See: (a) Jefferis, J. M.; Girolami, G. S. *Organometallics* **1998**, *17*, 3630–3632. (b) Jefferis, J. M.; Girolami, G. S. *Organometallics* **1999**, *18*, 3768–3768.

(46) Frapper, G.; Halet, J.-F. *Organometallics* **1995**, *14*, 5044–5053.

(47) (a) Geiser, U.; Kini, A. M. *Acta Crystallogr.* **1993**, *C49*, 1322–1324. (b) Martinengo, S.; Noziglia, L.; Fumagalli, A.; Albano, V. G.; Braga, D.; Grepioni, F. *J. Chem. Soc., Dalton Trans.* **1998**, 2493–2496.

(48) Li, J.; Schreckenbach, G.; Ziegler, T. *Inorg. Chem.* **1995**, *34*, 3245–3252.

(49) Eickerling, G.; Mastalerz, R.; Herz, V.; Scherer, W.; Himmel, H.-J.; Reiher, M. *J. Chem. Theory Comput.* **2007**, *3*, 2182–2197.

(50) (a) Pyykkö, P.; Declaux, J.-P. *Acc. Chem. Res.* **1979**, *12*, 276–281. (b) Schwarz, W. H. E.; van Wezenbeek, E. M.; Baerends, E. J.; Snijders, J. G. *J. Phys. B* **1989**, *22*, 1515–1530.

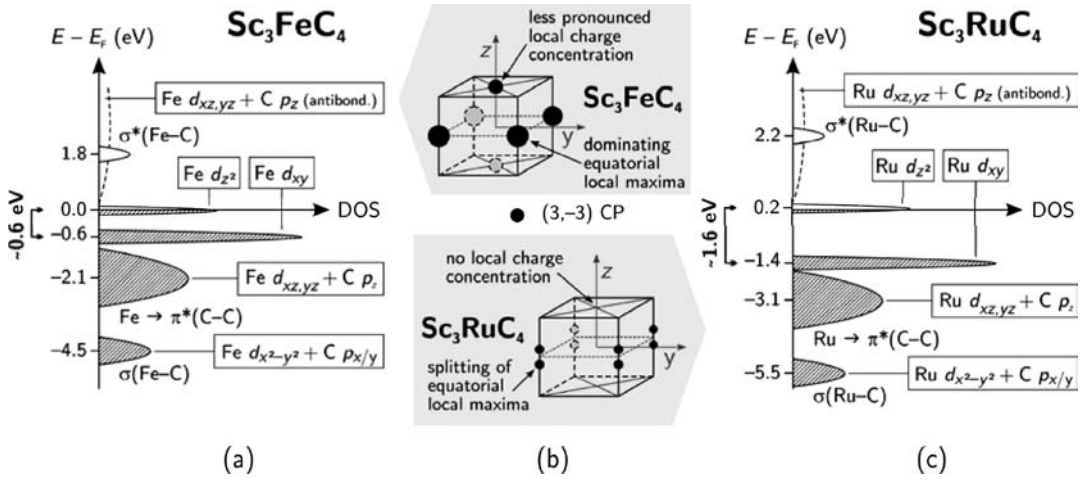

Figure 13. Relativistic and chemical bonding effects on the partial densities of states (DOS) of (a) Sc_3FeC_4 and (c) HT-Sc_3RuC_4 (simplified representation; for further details, see Figures 8−10). Subfigure b shows the positions of the charge concentrations in the valence shell of the Fe and Ru atoms with respect to the local coordinate system.

Comparison of the Bonding Situation in the HT and LT Phases of Sc_3RuC_4 and Sc_3OsC_4. We have demonstrated above that slow cooling procedures yielded 100 K data of LT-Sc_3RuC_4 and LT-Sc_3OsC_4 with high net intensities for the superstructure reflections, providing excellent data for subsequent structure refinements. However, the presence of twinning as a systematic consequence of the symmetry reduction on cooling (t2 transition) complicated experimental charge density studies. Hence, we employed theoretical charge density studies to trace the electronic and structural consequences of the phase transitions in Sc_3RuC_4 and Sc_3OsC_4 upon cooling (Table 6). As pointed out above, LT-Sc_3OsC_4 and its group 9 congener Sc_3IrC_4 form different superstructures. This fact suggests already at this stage of our analysis that it is the different electronic situation at the transition metal centers (d-electron count) which seems to control the nature of these structural phase transitions.

Comparison of the structures of the [TC_4] ribbons of Sc_3RuC_4 and Sc_3OsC_4 shows that the LT modifications are characterized by two sets of T−C and C−C bond distances due to the lowering of the local site symmetry at the metal from D_{2h} (HT phase) to C_s (LT phase). The major structural consequence is the loss of the horizontal mirror plane symmetry in the [TC_4] units (Figure 14) caused by a subtle square pyramidal distortion with an out-of-plane deviation of T by 7.70(6) for Ru and 7.67(2) pm for Os. As a result, we find acute valence angles ∠C(1)−T−C(1) = 87.3(2)° and 87.2(2)° and ∠C(2)−T−C(2) = 87.2(2)° and 87.1(2)° for T = Ru and Os, respectively. Note, that this type of distortion enhances the establishment of weak inter-ribbon Os−Os contacts of 316 pm (Figure 7) in the LT variant. Hence, the electronic driving force for the HT-LT transition—besides puckering effects (vide supra)—might be a Peierls-type crossover from isolated to pairwise assembled [TC_4] ribbons with noticeable interchain $T\cdots T$ interactions. However, the $T\cdots T$ contacts are still weak and not indicated by $T\cdots T$ BCPs in the charge density maps. Also the structural consequences inside the [$T(C2)_2$] ribbons are rather minute ($\triangle_{HT-LT}(T-C) \leq 0.6$ pm; $\triangle_{HT-LT}$(C−C) ≤ 0.9 pm). Accordingly, the corresponding topological parameters of the charge density, $\rho(\mathbf{r})$, at the bond critical points do not change significantly during the monoclinic distortion (Table 6). However, the subtle changes in the *local* electronic structure of the T metals during the LT−HT phase transition can be safely revealed by a topological analysis of the negative Laplacian of the charge density distribution, $L(\mathbf{r}) = -\nabla^2\rho(\mathbf{r})$. Bader et al. have demonstrated that the sign of $L(\mathbf{r})$ determines where charge density is *locally concentrated* ($L(\mathbf{r}) > 0$) or locally depleted ($L(\mathbf{r}) < 0$).[51] In addition, the $L(\mathbf{r})$ function can be employed to resolve the shell structure of atoms.[52] In general, the fourth, fifth, or sixth shell for elements of periods 4−6, respectively, is not revealed in the Laplacian.[53] As a convention, Bader et al. suggested that the outermost shell of charge concentration (CC) of an atom (the *second* shell of CC of the carbon atom, the *third* shell of CC of the iron, and the *fourth* shell of the ruthenium atom) represents its (effective) valence shell charge concentration (VSCC).[8b,54] Furthermore, in the presence of ligands, the VSCC of the transition metal center displays a fine structure—the so-called atomic graph—which is classified by its

(51) (a) Morse, P. M.; Feshbach, H. *Methods of Theoretical Physics, Part I*; McGraw-Hill: New York, 1953. (b) Bader, R. F. W.; MacDougall, P. J.; Lau, C. D. H. *J. Am. Chem. Soc.* **1984**, *106*, 1594–1605.

(52) (a) Bader, R. F. W.; Bedall, P. M. *J. Chem. Phys.* **1972**, *56*, 3320–3329. (b) Bader, R. F. W.; Essén, H. *J. Chem. Phys.* **1984**, *80*, 1943–1960.

(53) (a) Sagar, R. P.; Ku, A. C. T.; Smith, V. *J. Chem. Phys.* **1988**, *88*, 4367–4374. (b) Shi, Z.; Boyd, R. J. *J. Chem. Phys.* **1988**, *88*, 4375–4377. (c) Chan, W.-T.; Hamilton, I. P. *J. Chem. Phys.* **1998**, *108*, 2473–2485. Furthermore, four-component calculations on spherical symmetric atoms (Au) by Kohout et al. showed that the outermost shell of elements of period 6 might not be resolved in the second derivative of the radial density: (d) Kohout, M.; Savin, A.; Preuss, H. *J. Chem. Phys.* **1991**, *95*, 1928–1942. The Laplacian maps of Sc_3OsC_4 based on our Wien2k calculations do not resolve the n and $n-1$ shell of the osmium atoms. Charge density studies on 5d transition metals in molecular organometallic moieties came to similar results. Therefore, the failure of the $L(\mathbf{r})$ maps to reveal the n and $n-1$ shell of 5d transition metals seems to be a general phenomenon. For further information, see: (e) Eickerling, G.; Reiher, M. *J. Chem. Theory Comput.* **2008**, *4*, 286–296. See also:(f) Hebben, N.; Himmel, H.-J.; Eickerling, G.; Herrmann, C.; Reiher, M.; Herz, V.; Presnitz, M.; Scherer, W. *Chem. Eur. J.* **2007**, *13*, 10078–10087 and ref 48.

(54) (a) Bader, R. F. W.; Gillespie, R. J.; Martín, F. *Chem. Phys. Lett.* **1998**, *290*, 488–494. (b) McGrady, G. S.; Haaland, A.; Verne, H. P.; Volden, H. V.; Downs, A. J.; Shorokhov, D.; Eickerling, G.; Scherer, W. *Chem. Eur. J.* **2005**, *11*, 4921–4934.

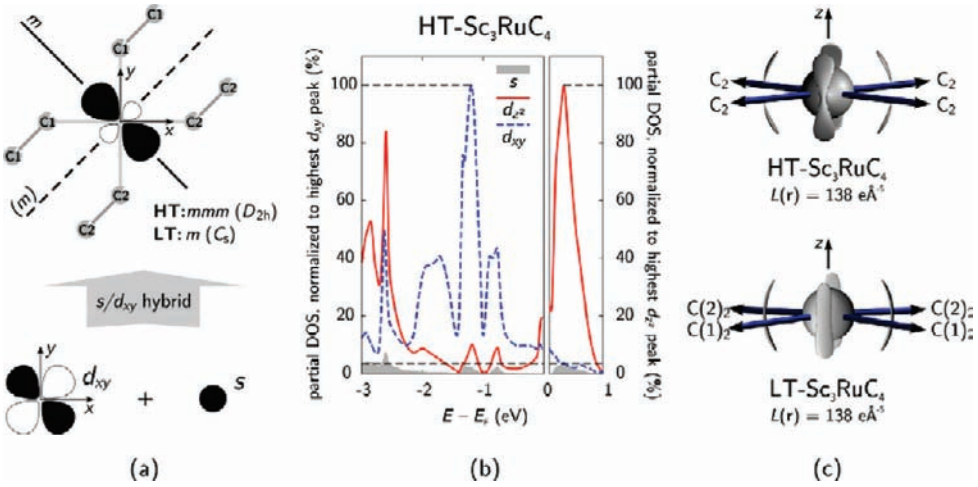

Figure 14. (a) Mixing of $T(n-1)\,d_{xy}$ and $T(n)$ s states allowed by symmetry in the HT (*mmm* or D_{2h} point symmetry) as well as in the LT (*m* or C_s point symmetry) variants of the $[TC_4]$ moieties. The (*n*) s contributions do not affect the nonbonding character of the d_{xy} states but lower their energy in the cases of T = Ru and Os due to relativistic effects. (b) Site- and state-projected partial DOS (WIEN2K results) of HT-Sc_3RuC_4; note that the DOS map is normalized to the highest d_{xy} ($E < E_F$) and d_{z^2} ($E > E_F$) peak, respectively. Therefore, a direct comparison of the relative s contribution to the d_{xy} and d_{z^2} states is possible. (c) Isosurface plots of the negative Laplacian around the Ru atom (WIEN2K results) in the HT and LT phases.

characteristic set of critical points [*V* (vertexes), *E* (edges), *F* (faces)].[55]

In the case of the Fe species, we experimentally observed six maxima of local charge concentration ($V = 6$) in an octahedral arrangement around the 3d metal center (Figure 13b). The four equatorial CCs are located in between the *T*−C bonds which define the *x* and approximately the *y* axis of our local coordinate system. Since, as shown above, the d_{xy} orbitals are not involved—for symmetry reasons—in the $\sigma(T \leftarrow C)$ donation and $T \rightarrow \pi^*(C-C)$ back-donation processes, they represent localized nonbonding orbitals. As a consequence, these localized states cause the sharp peak in the DOS at −0.6 eV (Figures 8 and 13a), while the Laplacian as a localization function[14,56] reveals the presence of these localized d electrons as four pronounced features between the Fe−C bonds in real space. In the same line, the two axial charge concentrations are correlated with the presence of localized nonbonding $d_{3z^2-r^2}$ states just below the Fermi energy (−0.1 eV).

The polarization pattern at the 3d metal iron [$V = 6$, $E = 12$, $F = 8$] changes dramatically in case of the 4d metal ruthenium in HT-Sc_3RuC_4. Figures 13b and 14 show that the local electronic structure at the Ru atom is now lacking an axial charge concentration. This change of the $L(\mathbf{r})$ topology can be related with the characteristic features of localized states in the DOS: the nonbonding $d_{3z^2-r^2}$ states—which were just below the Fermi energy in the case of the iron species—are shifted just above the Fermi level in the Ru case and are no longer significantly occupied (Figure 13c). As a consequence, no axial charge concentrations can be located in the $L(\mathbf{r})$ maps of Sc_3RuC_4. In the case of the LT variant of Sc_3RuC_4, we find a similar $L(\mathbf{r})$ topology at the metal center. A closer inspection of the $L(\mathbf{r})$ maps of both phases reveals a fine structure: in the HT case, each of the four equatorial charge concentrations is marginally split into two individual maxima, one above and one below the equatorial plane of the $[T(C_2)_2]$ moiety ([8,12,6] set of critical points). The splitting is less pronounced in the LT variant. We

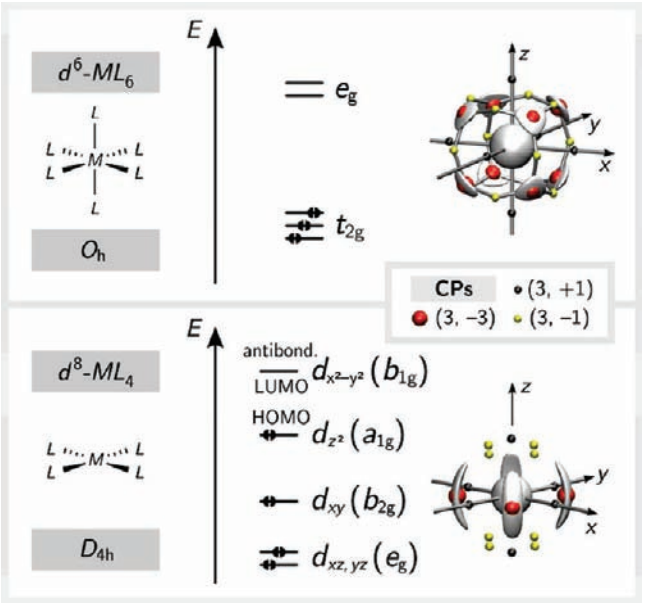

Figure 15. Correlation between the occupation of d orbitals and the resulting fine structure of the Laplacian in the valence shell of the transition metals in d^6-ML_6 and d^8-ML_4 complexes. (3, −3), (3, −1), and (3, +1) critical points in d^6-ML_6 (e.g., $Cr(CO)_6$ or $Mn(CO)_6^+$ displaying a cubic structure of local charge concentrations with a [8,12,6] set) and d^8-ML_4 complexes (e.g., $[Ni(NH_3)_4]^{2+}$ displaying a characteristic [4,8,6] set) are shown with large dark, small bright, and small dark spheres, respectively. For further details, see the Supporting Information.

(55) Local maxima or (3, −3) critical points (CPs) in $L(\mathbf{r})$ define the vertexes (*V*) of a polyhedron, while saddle points or (3, −1) CPs are located on the edges (*E*). Each of the resulting faces (*F*) depicts a (3, +1) CP which represents a local charge depletion zone. Note that the number of local maxima (*V*), saddle points (*E*), and local minima (*F*) fulfill Euler's relation: $V - E + F = 2$. See, for example: Bader, R. F. W.; Matta, C. F.; Cortés-Guzmán, F. *Organometallics* **2004**, *23*, 6253–6263.

(56) (a) Bader, R. F. W.; Heard, G. L. *J. Chem. Phys.* **1999**, *111*, 8789–8798. (b) Wagner, F. R.; Kohout, M.; Grin, Y. *J. Phys. Chem. A* **2008**, *112*, 9814–9828.

suggest that the splitting of the charge concentrations is a natural consequence of the increased $T-C$ bond strength in the case of T = Ru and Os, which in turn leads to a formally higher oxidation state of the transition metal centers. A higher oxidation state of the 4d metal would also be in line with the observed depopulation of nonbonding $d_{3z^2-r^2}$ states in the 4d metal carbide Sc_3RuC_4 relative to Sc_3FeC_4. Hence, the polarization pattern at the Ru atoms might be interpreted in terms of a crossover scenario between the formal oxidations states d^8 and d^6. For d^6 configured transition metals, a characteristic polarization pattern of eight charge concentrations (cuboidal arrangement) is typically observed and in line with the depletion of charge in the x, y, and z directions (unpopulated $d_{3z^2-r^2}$ and $d_{x^2-y^2}$ orbitals;[55,57] Figure 15). Hence, the topology of the Laplacian might be employed as a measure of the formal oxidation state of a transition metal atom—another result which warrants further exploration.[58]

To conclude, our study highlights that even tiny differences in the electronic structure of solids due to chemical bonding and relativistic effects might be faithfully recovered in the properties of the Laplacian of the electron density. In our case, small differences in the population of the nonbonding $d_{3z^2-r^2}$ states between the 3d carbide Sc_3FeC_4 and its 4d/5d congeners Sc_3RuC_4 and Sc_3OsC_4 are clearly reflected in the charge density picture by a significant change in the polarization pattern displayed by valence shell charge concentrations at the transition metal centers in the $[T(C_2)_2]$ units.

Acknowledgment. We thank Dr. F. M. Schappacher for the work at the scanning electron microscope, E. Hagemeier for the DSC measurements, and the Degussa-Hüls AG for a donation of ruthenium and osmium powder. This work was supported by the Deutsche Forschungsgemeinschaft within the priority programme SPP 1178.

Supporting Information Available: Crystallographic data in CIF format. Detailed comparison of the topological parameters at the critical points in the HT and LT variants of Sc_3TC_4 (T = Ru, Os). This material is available free of charge via the Internet at http://pubs.acs.org.

(57) (a) Bo, C.; Poblet, J. M.; Bernard, M. *Chem. Phys. Lett.* **1990**, *169*, 89–92. (b) Macchi, P.; Sironi, A. *Coord. Chem. Rev.* **2003**, *238*−*239*, 383–412. (c) Cortés-Guzmán, F.; Bader, R. F. W. *Coord. Chem. Rev.* **2004**, *249*, 633–662. (d) Farrugia, L. J.; Evans, C. *J. Phys. Chem. A.* **2005**, *109*, 8834–8848.

(58) We finally note that the CCs at the Ru metal center in the $[TC_4]$ plane are significantly smaller compared with its Fe analogue (ref 14) and even vanish in the case of the Sc_3OsC_4 (ref 52). This is also a consequence of the larger spatial extent of the 4d and 5d states as compared to the 3d states.